6-28-2016

Universal collisionless transport of graphene

Julia M. Link
Karlsruher Institut für Technologie

Peter P. Orth
Karlsruher Institut für Technologie

Daniel E. Sheehy
Louisiana State University

Jörg Schmalian
Karlsruher Institut für Technologie

Recommended Citation

Link, J., Orth, P., Sheehy, D., & Schmalian, J. (2016). Universal collisionless transport of graphene. *Physical Review B, 93* (23) https://doi.org/10.1103/PhysRevB.93.235447

Universal collisionless transport of graphene

Julia M. Link, Peter P. Orth, Daniel E. Sheehy, and Jörg Schmalian

Phys. Rev. B **93**, 235447 — Published 28 June 2016

DOI: 10.1103/PhysRevB.93.235447

Universal collisionless transport of graphene

Julia M. Link,[1] Peter P. Orth,[1,2] Daniel E. Sheehy,[3] and Jörg Schmalian[1,4]

[1] *Institute for Theory of Condensed Matter, Karlsruhe Institute of Technology (KIT), 76131 Karlsruhe, Germany*
[2] *School of Physics and Astronomy, University of Minnesota, Minneapolis, Minnesota 55455, USA*
[3] *Department of Physics and Astronomy, Louisiana State University, Baton Rouge, LA, 70803, USA*
[4] *Institute for Solid State Physics, Karlsruhe Institute of Technology (KIT), 76131 Karlsruhe, Germany*

(Dated: June 7, 2016)

The impact of the electron-electron Coulomb interaction on the optical conductivity of graphene has led to a controversy that calls into question the universality of collisionless transport in this and other Dirac materials. Using a lattice calculation that avoids divergences present in previous nodal Dirac approaches, our work settles this controversy and obtains results in quantitative agreement with experiment over a wide frequency range. We also demonstrate that dimensional regularization methods agree, as long as the scaling properties of the conductivity and the regularization of the theory in modified dimension are correctly implemented. Tight-binding lattice and nodal Dirac theory calculations are shown to coincide at low energies even when the non-zero size of the atomic orbital wave function is included, conclusively demonstrating the universality of the optical conductivity of graphene.

I. INTRODUCTION

In graphene, numerous electronic properties with energy sufficiently below the scale $v\Lambda \simeq 1-1.5\,\mathrm{eV}$ are governed by the linear Dirac spectrum with velocity v.[1] Examples are the minimal conductivity in disordered samples,[2] the odd-integer quantum Hall effect at high magnetic fields,[3] and the observation of Klein tunneling through potential barriers.[4] These observations are explained in terms of non-interacting Dirac fermions, while the electron-electron Coulomb interaction clearly affects other experimental results such as the fractional quantum Hall effect,[5,6] hydrodynamic transport behavior[7–12] and the logarithmically enhanced velocity, as seen in magneto-oscillation,[13] angular resolved photoemission spectroscopy[14] and capacitance measurements of the density of states.[15]

Given this success, it is remarkable that there exists a rather long-standing controversy in the theoretical description of Coulomb interaction corrections to the optical absorption of graphene.[16–24] Experiments report an optical transmission close to 97.7%,[25,26] a value that corresponds to non-interacting Dirac electrons. Considering Coulomb interactions within a renormalization group analysis, one finds for the optical conductivity ($\omega \ll v\Lambda$):

$$\sigma(\omega) = \sigma_0\left(1 + \mathcal{C}\alpha(\omega) + \cdots\right). \tag{1}$$

Here, $\sigma_0 = \pi e^2/(2h)$ is the universal value of the optical conductivity of non-interacting Dirac particles[27] and $\alpha(\omega) = \alpha/[1 + \frac{1}{4}\alpha\ln(v\Lambda/\omega)]$ is a running, renormalized, dimensionless coupling constant that measures the strength of the Coulomb interaction at the frequency scale ω, with bare value $\alpha \equiv \alpha(v\Lambda) = e^2/(\hbar v\epsilon)$.[28,29] Here, e is the electron charge and $\epsilon = (\epsilon_1+\epsilon_2)/2$ is determined by the dielectric constants $\epsilon_{1,2}$ of the material above and below the graphene sheet.

The value of the coefficient $\mathcal{C}$ is the issue of the controversy, with different theoretical approaches yielding different values for $\mathcal{C}$. The origin of these discrepancies can be traced to the low energy nodal Dirac approximation for graphene with linear spectrum $\varepsilon(\mathbf{q}) = \pm v|\boldsymbol{q}|$ for $|\boldsymbol{q}| \leq \Lambda$ with momentum cutoff Λ. A perturbative analysis of corrections due to Coulomb interactions to $\sigma(\omega)$ yields individual Feynman diagrams that are *logarithmically divergent* in the cutoff Λ. While these divergences cancel if one adds up all diagrams, the finite result, which determines $\mathcal{C}$, turns out to be different for different approaches to handle the divergences. Since $\sigma(\omega)$ determines the transmission coefficient $T(\omega) = (1+2\pi\sigma(\omega)/c)^{-2}$,[30] this issue is experimentally relevant and only a rather small value of $\mathcal{C}$ is consistent with current experimental observations.[18] These controversies were believed to be resolved when two of us demonstrated that a calculation that respects conservation of the electric charge leads to[18]

$$\mathcal{C} = \frac{19-6\pi}{12}, \tag{2}$$

a value that was first determined by Mishchenko.[17] The essential claim of Ref. 18 was that, while different results can be obtained within the nodal approximation (as found in earlier work[16]), this ambiguity is eliminated when the Ward identity is enforced.

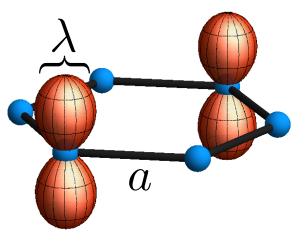

FIG. 1. (Color online) One plaquette of graphene's honeycomb lattice with blue spheres representing carbon atoms. The carbon-carbon distance is a and two electron p_z orbitals of typical width λ are illustrated.

However, subsequent investigations[19,20] led to an alternate result for $\mathcal{C}$, calling into question this picture. In particular, Juricic *et al.*[19] used the nodal approximation along with dimensional regularization of the integrals (altering the spatial dimension to $d = 2 - \epsilon$ with $\epsilon \to 0$ at the end of the calculation), obtaining a much larger value $\mathcal{C}' = (22 - 6\pi)/12$ within a calculation that also obeyed the Ward identity at least for finite ϵ. This larger value was also obtained in Ref. 20, who claimed to perform a tight-binding calculation. The authors of Ref. 20 concluded that the source of the error was the linearized spectrum and concluded that a proper treatment of the spectrum in the entire Brillouin zone (BZ) is needed to determine the optical conductivity. It was added that this unexpected behavior is related to a chiral anomaly or due to non-local optical effects.[31]

Given these discrepancies, an obvious question is whether $\mathcal{C}$ is indeed a universal number. If states in the entire BZ matter, one could easily construct new dimensionless quantities γ and the coefficient $\mathcal{C}$ in Eq. (1) might depend on γ. Then, distinct analytic results would merely correspond to different limits of $\mathcal{C}(\gamma)$. An example for such a dimensionless quantity is $\gamma = \lambda/a$, where $a \approx 1.42\,\text{Å}$ is the carbon-carbon distance and λ the characteristic size of the p_z-orbital Wannier function of the sp^2 hybridized carbon atoms in the graphene lattice (see Fig. 1). Then, only a detailed quantum chemical analysis would be able to determine the correct optical conductivity, even for frequencies small compared to the bandwidth. It would also imply that a formal renormalization procedure, as discussed in Ref. 32, would not suffice to generate a correct result, leading to a breakdown of the widely-used nodal approximation for graphene.

Here, we show that $\mathcal{C}$ is, in fact, a *universal* number that is independent of high-energy microscopic or cutoff dependent details. We demonstrate that it is given by the expression in Eq. (2) and that it can be correctly obtained within a low-energy effective nodal Dirac description of graphene. Our conclusions are based on two independent calculations: (i) an evaluation of the leading perturbative Coulomb correction to the optical conductivity using the full tight-binding graphene band structure. This unequivocally determines $\mathcal{C}$. It furthermore shows that $\mathcal{C}$ is universal and independent of, for example, the width of the atomic Wannier orbitals; (ii) a field-theoretical analysis of the interaction corrections to the conductivity within the Dirac description, which we use to demonstrate that the result for $\mathcal{C}$ is affected by the order of limits $d \to 2$ and cutoff $\Lambda \to \infty$. Taking the limits in the correct order yields the result of the lattice tight-binding calculation in (i).

Our main results are captured in Fig. 2, which shows the interaction correction coefficient obtained within the lattice tight-binding approach as a function of frequency ω. Clearly, the lattice result agrees with the numerical value $\mathcal{C}$ given in Eq. (2). Below, we also explain how to correctly obtain this value within the Dirac approximation of graphene using different regularization schemes.

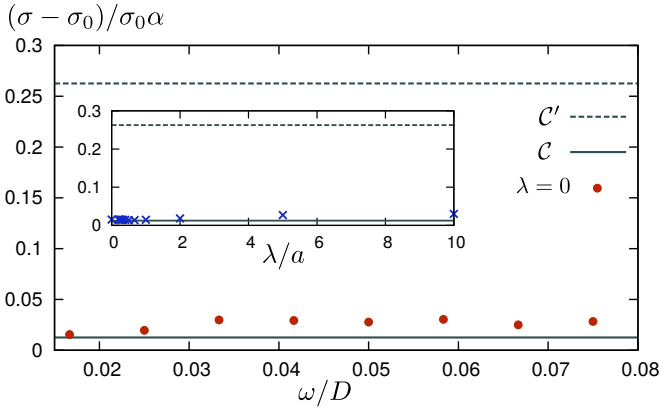

FIG. 2. (Color online) The main figure shows the interaction correction coefficient as determined by our lattice calculation (red dots) as a function of frequency ω/D, where D is the bandwidth of the lattice theory. The lattice result is in clear agreement with the predicted value Eq. (2) from nodal theory.[17,18] The inset shows that the result in the low-frequency limit ($\omega/D = 0.015$) is independent of the ratio λ/a (i.e., universal).

Furthermore, the inset of Fig. 2 proves that the interaction correction coefficient is universal and independent of the ratio λ/a, where λ is the size of the atomic orbitals on the graphene atoms and a is the lattice constant.

Below, we determine the correct value for $\mathcal{C}$ in Eq. (1), but also explain why other approaches failed to reach the correct conclusions. This should settle all aspects of the existing controversy about the value of $\mathcal{C}$. Our work demonstrates that the Dirac cone approximation can be safely applied for low energy properties, that the longitudinal optical conductivity is not affected by a chiral anomaly or states far from the Dirac cone and that no subtlety due to non-local effects in the conductivity occurs. Finally, we show how to properly include interaction corrections within the lattice theory, which is essential for physical quantities where a nodal approximation cannot be employed.

The remainder of the paper is organized as follows: in Sec. II, we start from a lattice tight-binding description of graphene and determine the optical conductivity, including leading Coulomb corrections, in the collisionless regime. Allowing for a finite extent of the Wannier functions λ, we demonstrate that $\mathcal{C}$ is indeed universal, i.e. independent of the ratio λ/a, and takes a value that is, within the numerical accuracy, given in Eq. (2). Further, we explain why previous lattice based attempts[20,31] failed to reach the correct conclusion.

A by-product of our calculation is the optical conductivity of non-interacting electrons in graphene for a nearest-neighbor tight-binding electronic band structure: $\sigma_0(\omega, \text{TB})$. This allows us to correct previously reported theoretical results of Refs. 25 and 30 and to demonstrate that $\sigma_0(\omega, \text{TB})$ deviates from the Dirac result more strongly than reported there. We compare the corrected theoretical prediction for the optical transmission $T(\omega)$

with the experimental data of Ref. 25.

In Sec. III, we show how to correctly obtain $\mathcal{C}$ within a field-theoretical description of graphene using the nodal Dirac approximation. We demonstrate that if one employs a Wilson momentum shell renormalization group approach and chooses to use dimensional regularization (in $d = 2 - \epsilon$ spatial dimensions) of divergent integrals, the interaction coefficient $\mathcal{C}$ acquires a dependence on the order of limits $\epsilon \to 0$ and ultraviolet cutoff $\Lambda \to \infty$ at the end of the calculation. The correct order of limits yields the same result for $\mathcal{C}$ as the lattice calculation.

Following earlier work by Teber *et al.* in Ref. 33, we show in Sec. III A that this ambiguity does not appear when, instead of the Wilson momentum shell renormalization group technique, one employs a different renormalization procedure and fully regularizes the theory within modified minimal subtraction $\overline{\text{MS}}$ scheme. Within the $\overline{\text{MS}}$ procedure of dimensional regularization, the non-interacting (bare-bubble) conductivity diagram contributes to the value of the interaction correction coefficient. This is the key difference to the work of Juricic *et al.* in Ref. 19 who also used dimensional regularization but only of the perturbative diagrams (instead of the full theory) and thus obtained the result $\mathcal{C}'$. Therefore, the apparent ambiguity in the value of the interaction coefficient is due to the fact that certain diagrams contributing to the conductivity give different results within different regularization schemes. In Sec. III B, we explore this and consider such diagrams in $d = 2 - \epsilon$ but including a ultraviolet cutoff Λ. We show that these diagrams only combine to give the correct value for $\mathcal{C}$ when the order of limits ($\epsilon \to 0$ and $\Lambda \to \infty$) is correctly taken.

We conclude in Sec. IV and refer to the Appendices for details of a number of calculations that are discussed in the main text.

II. THE TIGHT-BINDING APPROACH TO THE OPTICAL CONDUCTIVITY

In this section, we calculate the self-energy $\Sigma(\boldsymbol{k})$ and the optical conductivity $\sigma(\omega)$ to leading order in perturbation theory within a full lattice approach that considers the nearest-neighbor tight-binding energy spectrum of graphene. We begin in Sec. II A by defining the non-interacting lattice Hamiltonian H_0, the bare lattice Green's function $G_{\boldsymbol{k},i\omega}$ and the current operator $\boldsymbol{J}_{\boldsymbol{k}}$ on the lattice. In Sec. II B, we derive the Coulomb interaction Hamiltonian on the graphene lattice. In Sec. II C, we use it to calculate the electronic self energy $\Sigma(\boldsymbol{k})$ on the lattice, which describes the renormalization of the Fermi velocity due to interactions. In Sec. II D, we numerically compute the optical conductivity $\sigma(\omega)$ using the Kubo formula in a full lattice description: in Sec. II D 1 we first obtain the non-interacting result $\sigma_0(\omega)$, before we calculate, in Sec. II D 2, the lowest-order corrections due to Coulomb interactions.

A. Single-particle Hamiltonian and current operator on the lattice

Graphene is a honeycomb lattice of carbon atoms spanned by the triangular Bravais lattice vectors $\boldsymbol{R}_i = i_1\boldsymbol{a}_1 + i_2\boldsymbol{a}_2$ with $i_{1,2} \in \mathbb{Z}$, primitive vectors $\boldsymbol{a}_{1,2} = \frac{\sqrt{3}}{2}a(\pm 1, \sqrt{3})$, and basis vectors $\boldsymbol{v}_{1,2}$. One choice is $\boldsymbol{v}_1 = 0$, $\boldsymbol{v}_2 = (0, -a)$ as can be seen in Fig. 3. The electron creation operators $c^\dagger_{\boldsymbol{R}_i\ell\sigma}$ create an electron with spin σ on the corresponding lattice site $(\boldsymbol{R}_i, \ell)$ with $\ell = 1, 2$ denoting the basis site $\boldsymbol{v}_\ell$. We often write $c^\dagger_{\boldsymbol{R}_i 1\sigma} \equiv a^\dagger_{\boldsymbol{R}_i\sigma}$ for $\ell = 1$ and $c^\dagger_{\boldsymbol{R}_i 2\sigma} \equiv b^\dagger_{\boldsymbol{R}_i\sigma}$ for $\ell = 2$, and introduce a spinor composed of electron creation operators on the two basis sites as

$$c^\dagger_{\boldsymbol{R}_i\sigma} = (c^\dagger_{\boldsymbol{R}_i 1\sigma}, c^\dagger_{\boldsymbol{R}_i 2\sigma}) = (a^\dagger_{\boldsymbol{R}_i\sigma}, b^\dagger_{\boldsymbol{R}_i\sigma})\,. \tag{3}$$

With these definitions it follows that the tight-binding Hamiltonian reads

$$H_0 = \sum_{\boldsymbol{k}\ell\ell'\sigma} c^\dagger_{\boldsymbol{k}\ell\sigma}\mathcal{H}_{\boldsymbol{k}\ell\ell'}c_{\boldsymbol{k}\ell'\sigma}\,, \tag{4}$$

with $c_{\boldsymbol{R}_i\ell\sigma} = \frac{1}{\sqrt{N}}\sum_{\boldsymbol{k}} e^{i\boldsymbol{k}\boldsymbol{R}_i}c_{\boldsymbol{k}\ell\sigma}$. In case of only nearest-neighbor hopping t, one finds $\mathcal{H}_{\boldsymbol{k}} = -t\,\boldsymbol{h}_{\boldsymbol{k}}\cdot\boldsymbol{\sigma}$ with the vector $\boldsymbol{h}_{\boldsymbol{k}} = (\operatorname{Re} h_{\boldsymbol{k}}, -\operatorname{Im} h_{\boldsymbol{k}})$ given by $h_{\boldsymbol{k}} = 1 + e^{i\boldsymbol{k}\boldsymbol{a}_1} + e^{i\boldsymbol{k}\boldsymbol{a}_2}$ and Pauli matrices $\boldsymbol{\sigma} = (\sigma_x, \sigma_y)$. Explicitly, this reads

$$\mathcal{H}_{\boldsymbol{k}} = -t\begin{pmatrix} 0 & h_{\boldsymbol{k}} \\ h^*_{\boldsymbol{k}} & 0\end{pmatrix}\,, \tag{5}$$

with $h_{\boldsymbol{k}} = 1 + 2\cos\left(\frac{\sqrt{3}}{2}k_x a\right)e^{i\frac{3}{2}k_y a}$. The energy spectrum consists of two bands with energy $\varepsilon_{\boldsymbol{k}\pm} = \pm t|h_{\boldsymbol{k}}|$, and a linear Dirac spectrum emerges near the Dirac points $\mathbf{K}_\pm = \frac{2\pi}{3a}(\pm\frac{1}{\sqrt{3}}, 1)$. The bare Green's function is given by $G_{\boldsymbol{k},i\omega} = (i\omega - \mathcal{H}_{\boldsymbol{k}})^{-1}$, and reads explicitly

$$G_{\boldsymbol{k},i\omega} = \frac{1}{\omega^2 + t^2|h_{\boldsymbol{k}}|^2}\begin{pmatrix} -i\omega & th_{\boldsymbol{k}} \\ th^*_{\boldsymbol{k}} & -i\omega\end{pmatrix}. \tag{6}$$

The current operator follows via the usual Peierls substitution $t \to te^{ie\boldsymbol{A}\boldsymbol{u}_\alpha}$ of the hopping element to the nearest-neighbor site at $\boldsymbol{u}_\alpha$ from taking the derivative $\boldsymbol{J} = -(\partial_{\boldsymbol{A}}H_0)|_{\boldsymbol{A}=0}$. Alternatively, it can be found from $\boldsymbol{J} = i[H_0, \boldsymbol{P}]$ with polarization operator $\boldsymbol{P} = \sum_{\boldsymbol{R}_i,\ell,\sigma}(\boldsymbol{R}_i + \boldsymbol{v}_\ell)c^\dagger_{\boldsymbol{R}_i\ell\sigma}c_{\boldsymbol{R}_i\ell\sigma}$.[34] In both ways, one finds

$$\boldsymbol{J}_{\boldsymbol{R}_i} = -\frac{iet}{\hbar}\sum_{\boldsymbol{\delta}_\alpha}[(\boldsymbol{\delta}_\alpha + \boldsymbol{v}_2 - \boldsymbol{v}_1)b^\dagger_{\boldsymbol{R}_i+\boldsymbol{\delta}_\alpha}a_{\boldsymbol{R}_i} - \text{h.c.}] \tag{7}$$

with nearest-neighbor Bravais lattice vectors $\boldsymbol{\delta}_\alpha \in \{(0,0), \boldsymbol{a}_1, \boldsymbol{a}_2\}$. In momentum space, it takes the form

$$\boldsymbol{J}_{\boldsymbol{k}} = \sum_{\boldsymbol{k},\ell,\ell',\sigma} c^\dagger_{\boldsymbol{k}\ell\sigma}\begin{pmatrix} 0 & \boldsymbol{j}_{\boldsymbol{k}} \\ \boldsymbol{j}^*_{\boldsymbol{k}} & 0\end{pmatrix}_{\ell\ell'} c_{\boldsymbol{k}\ell'\sigma} \tag{8}$$

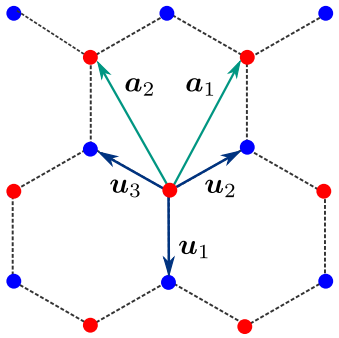

FIG. 3. (Color online) Honeycomb crystal lattice of graphene, showing two interpenetrating (red and blue) sublattices of carbon atoms. The Bravais lattice with lattice vectors $\boldsymbol{R}_i = i_1\boldsymbol{a}_1 + i_2\boldsymbol{a}_2$ is defined to be the red sublattice, with a two-atom basis defined by $\boldsymbol{v}_1 = 0$ (the red points) and $\boldsymbol{v}_2 = -a\hat{y}$ (the blue points), where a is the carbon-carbon distance. The three nearest-neighbor vectors are $\boldsymbol{u}_\alpha = \boldsymbol{\delta}_\alpha + \boldsymbol{v}_2 - \boldsymbol{v}_1$ with nearest-neighbor Bravais vectors $\boldsymbol{\delta}_1 = (0,0)$, $\boldsymbol{\delta}_2 = \boldsymbol{a}_1$ and $\boldsymbol{\delta}_3 = \boldsymbol{a}_2$.

with explicit components

$$j_{x,\boldsymbol{k}} = \sqrt{3}tae\sin\Big(\frac{\sqrt{3}}{2}k_x a\Big)e^{i\frac{3}{2}k_y a} \tag{9}$$

$$j_{y,\boldsymbol{k}} = -itae\Big[\cos\Big(\frac{\sqrt{3}}{2}k_x a\Big)e^{i\frac{3}{2}k_y a} - 1\Big]\,. \tag{10}$$

In the following, we often set $e = a = 1$, since it can be easily reinstated in the final result.

B. The Coulomb interaction Hamiltonian

Electrons interact via the Coulomb interaction, which is described by the Hamiltonian

$$H_{int} = \frac{e^2}{2}\sum_{\sigma\sigma'}\int d^3r\, d^3r'\,\frac{\psi^\dagger_{\boldsymbol{r}\sigma}\psi^\dagger_{\boldsymbol{r}'\sigma'}\psi_{\boldsymbol{r}'\sigma'}\psi_{\boldsymbol{r}\sigma}}{\epsilon|\boldsymbol{r}-\boldsymbol{r}'|}\,, \tag{11}$$

where $\boldsymbol{r}, \boldsymbol{r}'$ are three-dimensional real-space position vectors, i.e. $\boldsymbol{r} = (\boldsymbol{\rho}, z)$ with $\boldsymbol{\rho} = (x, y)$. The graphene sheet is assumed to be located in the x-y-plane with $z = 0$. The field operators

$$\psi_{\boldsymbol{r}\sigma} = \sum_{\boldsymbol{R}_i,\ell}\varphi(\boldsymbol{r}-\boldsymbol{R}_i-\boldsymbol{v}_\ell)c_{\boldsymbol{R}_i\ell\sigma} \tag{12}$$

are defined via the Wannier p_z-atomic orbitals $\varphi(\boldsymbol{r})$ localized on the sp^2-hybridized carbon atoms at sites $(\boldsymbol{R}_i, \ell)$. In the evaluation of the Coulomb matrix elements, i.e. when Eq. (12) is inserted into Eq. (11), we assume that $\varphi^*(\boldsymbol{r}-\boldsymbol{R}_i-\boldsymbol{v}_\ell)\varphi(\boldsymbol{r}-\boldsymbol{R}_j-\boldsymbol{v}_{\ell'})$ is small unless $i = j$ and $\ell = \ell'$. The density of spin σ is thus approximated by

$$\psi^\dagger_{\boldsymbol{r}\sigma}\psi_{\boldsymbol{r}\sigma} \approx \sum_{\boldsymbol{R}_i,\ell} c^\dagger_{\boldsymbol{R}_i\ell\sigma}c_{\boldsymbol{R}_i\ell\sigma}|\varphi(\boldsymbol{r}-\boldsymbol{R}_i-\boldsymbol{v}_\ell)|^2\,. \tag{13}$$

Using this approximation, and inserting the Fourier transform of the real-space Coulomb interaction $\frac{e^2}{\epsilon|\boldsymbol{r}-\boldsymbol{r}'|} = \int\frac{d^2q}{(2\pi)^2}\int\frac{dq_z}{2\pi}\mathrm{e}^{i\boldsymbol{q}\cdot(\boldsymbol{\rho}-\boldsymbol{\rho}')}\mathrm{e}^{iq_z(z-z')}\frac{4\pi e^2}{\epsilon(q^2+q_z^2)}$, we obtain

$$H_{int} = \int_{\substack{r,r'\\q,q_z}} e^{i\boldsymbol{q}(\boldsymbol{\rho}-\boldsymbol{\rho}')}e^{iq_z(z-z')}\frac{4\pi e^2}{\epsilon(q^2+q_z^2)}\sum_{\substack{\boldsymbol{R}_i,\boldsymbol{R}_j\\\ell,\ell'}}|\varphi(\boldsymbol{r}-\boldsymbol{R}_i-\boldsymbol{v}_\ell)|^2|\varphi(\boldsymbol{r}'-\boldsymbol{R}_j-\boldsymbol{v}_{\ell'})|^2c^\dagger_{\boldsymbol{R}_i\ell\sigma}c^\dagger_{\boldsymbol{R}_j\ell'\sigma'}c_{\boldsymbol{R}_j\ell'\sigma'}c_{\boldsymbol{R}_i\ell\sigma}\,, \tag{14}$$

where $\int_r = \int d^3r$, $\int_q = \int\frac{d^2q}{(2\pi)^2}$ and $\int_{q_z} = \int\frac{dq_z}{2\pi}$. To evaluate the integration over r and r', we shift $\boldsymbol{r}\to\boldsymbol{r}+\boldsymbol{R}_i+\boldsymbol{v}_\ell$ and similarly for $\boldsymbol{r}'$, an operation that introduces phase factors of the form $\mathrm{e}^{i\boldsymbol{q}\cdot(\boldsymbol{R}_i+\boldsymbol{v}_\ell)}$. The summations over $\boldsymbol{R}_i$ and $\boldsymbol{R}_j$ then implement lattice Fourier transforms on the operators $c_{\boldsymbol{R}_i\ell\sigma}$, leading to

$$H_{int} = \frac{1}{2}\int\frac{d^2q}{(2\pi)^2}V(\boldsymbol{q})\sum_{\ell,\ell'}e^{i\boldsymbol{q}(\boldsymbol{v}_l-\boldsymbol{v}_{l'})}\sum_{\boldsymbol{k}\boldsymbol{k}'\sigma\sigma'}c^\dagger_{\boldsymbol{k}+\boldsymbol{q}\ell\sigma}c^\dagger_{\boldsymbol{k}'-\boldsymbol{q}\ell'\sigma'}c_{\boldsymbol{k}'\ell'\sigma'}c_{\boldsymbol{k}\ell\sigma}\,. \tag{15}$$

In the following, we will often incorporate the summation over ℓ, ℓ' as a matrix multiplication and introduce the matrix

$$M_{\boldsymbol{q}} = \begin{pmatrix}\exp(i\boldsymbol{q}\boldsymbol{v}_1) & 0\\ 0 & \exp(i\boldsymbol{q}\boldsymbol{v}_2)\end{pmatrix}\,. \tag{16}$$

In physical terms, it accounts for the spatial separation of the two carbon basis atoms and renders integration over momentum $\boldsymbol{q}$ finite. The Coulomb interaction matrix element in Eq. (15)

$$V(\boldsymbol{q}) = 4\pi e^2\int_{-\infty}^{\infty}\frac{dq_z}{2\pi}\frac{|\rho(\boldsymbol{q},q_z)|^2}{\epsilon(q^2+q_z^2)} \tag{17}$$

is determined by the electron density of the three-dimensional atomic orbital $\rho(\mathbf{q},q_z) = \int d^3r\,|\varphi(\boldsymbol{r})|^2\,e^{i(\boldsymbol{q}\boldsymbol{\rho}+q_z z)}$. Using the $2p_z$-orbitals with effective Bohr radius a_B^*, we obtain $V(\boldsymbol{q}) = 2\pi e^2\mathcal{F}(\boldsymbol{q})/(\epsilon|\boldsymbol{q}|)$, where the form factor was fitted to $\mathcal{F}(\boldsymbol{q}) = \exp(-|\boldsymbol{q}|a_B^*)$ and $a_B^* \simeq 0.9$Å.[35] In the following, we use the phe-

nomenological form

$$V(\boldsymbol{q}) = 2\pi e^2 \frac{\exp\left(-|\boldsymbol{q}|^2\lambda^2/2\right)}{\epsilon|\boldsymbol{q}|} \tag{18}$$

that follows from an orbital wavefunction that has Gaussian shape in the graphene plane and is point like in the z-direction: $\varphi(\boldsymbol{r}) = \varphi(x,y,z) = \delta(z)\frac{1}{\lambda\sqrt{\pi}}\exp\left[-(x^2+y^2)/2\lambda^2\right]$. Here, λ corresponds to the characteristic size of the orbital (see Fig. 1). In the limit of point like atomic orbitals $\lambda \to 0$, we find $V(\boldsymbol{q}) = 2\pi e^2/(\epsilon|\boldsymbol{q}|)$.

An important remark is that all momentum vectors in Eq. (15) are two-dimensional. Crucial for our subsequent analysis is the fact that the sums $\sum_{\boldsymbol{k},\boldsymbol{k}'}$ in Eq. (15) run over the first BZ, while the integral over $\boldsymbol{q}$ goes over the infinite momentum space, i.e., it is a combined sum over transferred momenta of the BZ and a sum over all reciprocal lattice vectors. This distinction was ignored in earlier work;[20] see, however, Ref. 21 for a discussion of this issue. This follows from the fact that the electron density of the orbitals $|\varphi(\boldsymbol{r})|^2$ is not confined to the discrete lattice points.

C. Electronic self-energy on the lattice

Before turning to the optical conductivity, let us investigate the electronic self-energy $\Sigma(\boldsymbol{k})$ within the lattice tight-binding formulation. We note that within the nodal Dirac approximation of graphene, the self-energy explicitly depends on the momentum cutoff Λ.[28,29] In a lattice theory an ultraviolet cutoff is naturally provided by the inverse lattice constant $1/a$. We thus expect that the self-energy does not exhibit any ultraviolet divergences despite the fact that it involves an (infinite) momentum integration. In this section, we verify this directly by explicitly evaluating the self-energy on the lattice.

The self-energy arising from Eq. (15) follows in standard perturbation theory as

$$\Sigma(\boldsymbol{k}) = -\int \frac{d^2q}{(2\pi)^2} V(\boldsymbol{q}) T \sum_{\omega} M_{-\boldsymbol{q}} G_{\boldsymbol{k}+\boldsymbol{q},i\omega} M_{\boldsymbol{q}}\,, \tag{19}$$

where the matrix $M_{\boldsymbol{q}}$ is defined below Eq. (16) and the bare Green's function is given in Eq. (6). Evaluating the frequency integration yields $\Sigma(\boldsymbol{k}) = \begin{pmatrix} 0 & \Sigma_{12} \\ \Sigma_{12}^* & 0 \end{pmatrix}$ with

$$\Sigma_{12}(\boldsymbol{k}) = -\frac{1}{2}\int \frac{d^2q}{(2\pi)^2} V(\boldsymbol{q}) e^{i\phi(\boldsymbol{k}+\boldsymbol{q})} e^{i\boldsymbol{q}(\boldsymbol{v}_2-\boldsymbol{v}_1)} \tag{20}$$

and $\exp[i\phi(\boldsymbol{k})] = h_{\boldsymbol{k}}/|h_{\boldsymbol{k}}|$. In order to show that the integration over momentum $\boldsymbol{q}$ yields a finite result, we first notice that the momentum argument $\boldsymbol{k}$ of the self-energy lies in the first Brillouin zone (BZ) (see Eq. (15)). The self-energy is periodic in reciprocal lattice vectors $\boldsymbol{G}$, i.e. $\Sigma(\boldsymbol{k}+\boldsymbol{G}) = \Sigma(\boldsymbol{k})$, and performing a Fourier transformation to real-space yields the self-energy as a function of Bravais lattice vectors

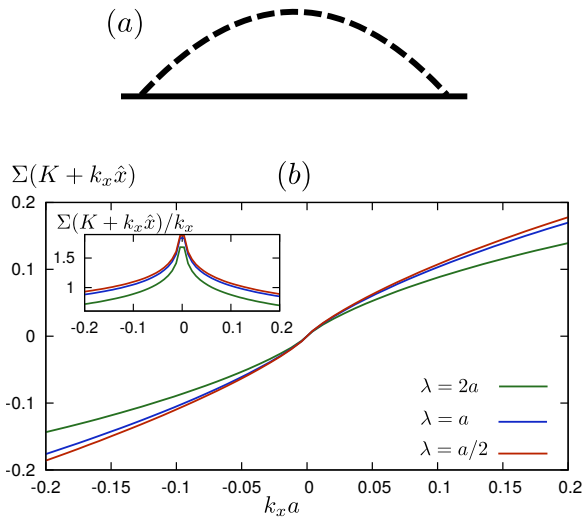

FIG. 4. (Color online) (a) Feynman diagram of the electronic self-energy. Dashed line corresponds to Coulomb interaction and solid line to bare Green's function. (b) Lattice self-energy $\Sigma(\boldsymbol{k})$ for momentum close to the Dirac node $K \equiv K_+$ for different Wannier orbital sizes λ/a. The inset shows the logarithmic divergence of the slope (= velocity correction) close to the node.

$$\Sigma_{12}(\boldsymbol{R}_i) = \sum_{\boldsymbol{k}} \Sigma_{12}(\boldsymbol{k}) e^{-i\boldsymbol{k}\cdot\boldsymbol{R}_i}\,. \tag{21}$$

The back transformation is explicitly given by $\Sigma_{12}(\boldsymbol{k}) = A\sum_{\boldsymbol{R}_i} e^{i\boldsymbol{k}\cdot\boldsymbol{R}_i}\Sigma_{12}(\boldsymbol{R}_i)$, where $A = \frac{3\sqrt{3}}{2}a^2$ is the unit-cell area. We insert Eq. (20) into Eq. (21), switch the order of integration and shift $\boldsymbol{k} \to \boldsymbol{k}' = \boldsymbol{k}+\boldsymbol{q}$, which is valid as the integrand is periodic under $\boldsymbol{k} \to \boldsymbol{k}+\boldsymbol{G}$, to arrive at

$$\Sigma_{12}(\boldsymbol{R}) = -\frac{1}{2}\int \frac{d^2q}{(2\pi)^2} V(\boldsymbol{q}) e^{i\boldsymbol{q}\cdot(\boldsymbol{R}_i+\boldsymbol{v}_2-\boldsymbol{v}_1)} F(\boldsymbol{R}_i) \tag{22}$$

with function

$$F(\boldsymbol{R}_i) = \sum_{\boldsymbol{k}'} e^{i[\phi(\boldsymbol{k}')-\boldsymbol{k}'\cdot\boldsymbol{R}_i]}\,. \tag{23}$$

Note that the momentum summation in Eq. (23) is restricted to the first Brillouin zone and can thus be conveniently performed numerically. The advantage of this transformation to real-space is that it allows to perform the (infinite) momentum integration over $\boldsymbol{q}$ exactly. This integration is the Fourier transform of the Coulomb interaction potential $V(\boldsymbol{q})$ evaluated at position $\boldsymbol{R}_i+\boldsymbol{v}_2-\boldsymbol{v}_1$. It thus depends on the form of the Wannier functions $\varphi(\boldsymbol{r})$ (see Eq. (17)). Using point like Wannier orbitals, i.e. $\lambda \to 0$ in Eq. (21), the integration over $\boldsymbol{q}$ simply returns the real-space Coulomb interaction and the self-energy in momentum space is given by

$$\Sigma_{12}(\boldsymbol{k}) = -\frac{e^2}{2\epsilon} A \sum_{\boldsymbol{R}_i} e^{i\boldsymbol{k}\cdot\boldsymbol{R}_i} \frac{1}{|\boldsymbol{R}_i+\boldsymbol{v}_2-\boldsymbol{v}_1|} F(\boldsymbol{R}_i)\,. \tag{24}$$

We have thus traded a numerically intensive infinite momentum integration over $\boldsymbol{q}$ for an infinite sum over Bravais lattice vectors $\boldsymbol{R}_i$. It turns out that the function $F(\boldsymbol{R}_i)$ decays sufficiently fast as a function of $|\boldsymbol{R}_i|$ such that the sum can be numerically evaluated to great precision. In all our presented results (see Figs. 2, 4, 7, and 8), the real-space summations run over the 4.6×10^4 Bravais lattice vectors $\boldsymbol{R}_i$ of smallest magnitude.

Considering a finite in-plane width of the Wannier orbitals $\lambda > 0$, the self-energy takes the form

$$\Sigma_{12}(\boldsymbol{k}) = -\frac{e^2}{2\epsilon}\frac{A}{\lambda}\sum_{\boldsymbol{R}_i} e^{i\boldsymbol{k}\cdot\boldsymbol{R}_i}\sqrt{\frac{\pi}{2}}e^{-|\boldsymbol{R}_i+\boldsymbol{v}_2-\boldsymbol{v}_1|^2/(4\lambda^2)} \times I_0\Big(\frac{|\boldsymbol{R}_i+\boldsymbol{v}_2-\boldsymbol{v}_1|^2}{4\lambda^2}\Big)F(\boldsymbol{R}_i)\,, \qquad (25)$$

where $I_0(x)$ is the modified Bessel function of the first kind. Clearly, Eq. (25) reduces to Eq. (24) in the limit $\lambda \ll a$.

It is clear from Eq. (24) that a potential divergence in $\Sigma_{12}(\boldsymbol{k})$ cannot come from the short distance behavior of the Coulomb interaction (since the denominator of $\frac{1}{|\boldsymbol{R}+\boldsymbol{v}_2-\boldsymbol{v}_2|}$ never reaches zero) but only relies on the convergence of the sum at large $\boldsymbol{R}_i$. This convergence can be traced back as being due to the factor $e^{i\boldsymbol{q}(\boldsymbol{v}_2-\boldsymbol{v}_1)}$ in Eq. (20) that oscillates rapidly at large $|q|$, causing the integral to vanish at large $|q|$. However, we find that the *slope* of $\Sigma_{12}(\boldsymbol{k})$ close to the Dirac nodes $\boldsymbol{K}_\pm$ exhibits a logarithmic divergence. This is shown in Fig. 4(b) and is a well known property found in the Dirac approximation that we now see holds in the full tight-binding theory as well. We observe in the inset of Fig. 4(b) that different Wannier orbital widths only affect the prefactor of the logarithm. As we show below, one of the two main contributions to the conductivity relies on determining $\Sigma_{12}(\boldsymbol{k})$ for all momenta in the BZ by computing the sum in Eq. (24).

D. Optical conductivity

We determine the real part of the optical conductivity via the Kubo formula

$$\sigma(\omega) = -\frac{\mathrm{Im}\chi_J(\omega)}{\omega}\,, \qquad (26)$$

where $\chi_J(\omega)$ is the retarded current-current response function. A detailed derivation of the Kubo formula can be found in Appendix A. Expanding perturbatively in orders of the Coulomb interaction strength α gives $\chi_J = \chi_J^{(0)} + \chi_J^{(1)} + \ldots$, where $\chi_J^{(0)}$ refers to non-interacting electrons (see diagram (a) in Fig. 5). The term $\chi_J^{(1)}$ is the leading order interaction correction depicted in Fig. 5 (b-d) with self-energy (b,c) and vertex (d) parts, giving rise to contributions $\chi_J^{(1,bc)}$ and $\chi_J^{(1,d)}$ calculated below. The optical conductivity σ and the interaction correction coefficient $\mathcal{C}$ are then determined by adding all contributions as $\sigma = \sigma^{(0)} + \sigma^{(1)} + \ldots$ with $\sigma^{(i)} = -\mathrm{Im}\chi_J^{(i)}/\omega$.

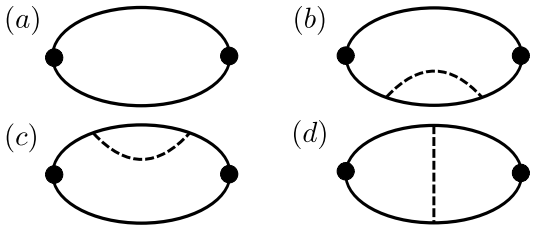

FIG. 5. Panel (a) shows the Feynman diagram for the non-interacting current-current correlation function $\chi_J^{(0)}$. Panels (b) – (d) show the lowest order Coulomb interaction corrections: (b) – (c) are self-energy diagrams and (d) the vertex correction.

In the following, in Sec. II D 1 we first evaluate the lattice expressions for non-interacting electrons $\chi_J^{(0)}$. In Sec. II D 2 we then turn to the calculation of the interaction corrections $\chi_J^{(1)}$.

1. *Result for non-interacting electrons*

The optical conductivity for non-interacting electrons is determined by the free current-current response function $\chi_J^{(0)}$, which is diagramatically shown in Fig. 5(a) and reads

$$\chi_J^{(0)}(i\omega) = -\frac{T}{2}\sum_{\boldsymbol{k},\epsilon,\nu}\mathrm{Tr}\big[J_{\boldsymbol{k}\nu}G_{\boldsymbol{k},i\epsilon}J_{\boldsymbol{k}\nu}G_{\boldsymbol{k},i\epsilon+i\omega}\big] = -\frac{1}{2}\sum_{\boldsymbol{k},\nu}\frac{\big(h^*_{\boldsymbol{k}}j_{\nu,\boldsymbol{k}} - h_{\boldsymbol{k}}j^*_{\nu,\boldsymbol{k}}\big)^2}{t\;|h_{\boldsymbol{k}}|(4|h_{\boldsymbol{k}}|^2+\omega^2/t^2)}. \qquad (27)$$

We evaluate $\chi_J^{(0)}$ by first analytically continuing $i\omega \to \omega + i\delta$ and then computing the remaining one-dimensional integral. A straightforward numerical evaluation yields

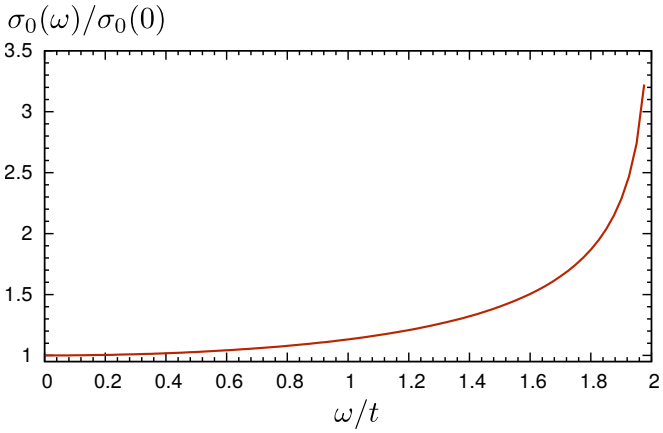

FIG. 6. (Color online) Conductivity $\sigma_0(\omega)$ for non-interacting electrons, obtained within the lattice nearest-neighbor tight-binding calculation and normalized to its value at zero frequency.

the result shown in Fig. 6, which shows that the (zero-frequency) Dirac result $\sigma(0) = \sigma_0 = e^2/(4\hbar)$ (for spinful electrons) is valid for $\omega \ll t$ and breaks down close to the van-Hove singularity at $\omega = 2t$. We also evaluate $\sigma(\omega)$ analytically by expanding perturbatively in small ω/t to arrive at (for details see Appendix A 1)

$$\sigma(\omega) = \frac{\pi}{32\omega}\rho\left(\frac{\omega}{2}\right)(18+\omega^2) - \frac{1}{8}\frac{\omega^2}{36} \tag{28}$$

$$\approx \sigma_0\left(1 + \frac{1}{9}\omega + \mathcal{O}(\omega^3)\right). \tag{29}$$

Here, we have set $t = 1$ and used that the density of states is given by

$$\rho(E) = \frac{1}{(2\pi)^2}\frac{32E\sqrt{1-\frac{E}{3}}K\left[\frac{-16E}{(E-3)(1+E)^3}\right]}{3(3-E)(1+E)^{3/2}}. \tag{30}$$

Here, $K[m]$ is the complete elliptic integral of the first kind. Importantly, beyond the Dirac approximation our results differ from previously reported ones.[25,30] As shown in Fig. 8 below this has consequences for the experimentally observable optical transmission through graphene, which differs more strongly from the non-interacting Dirac limit than previously reported.

2. *Interaction corrections to the optical conductivity*

In this section, we determine the leading order interaction correction to the optical conductivity $\chi_J^{(1)}$. The corresponding Feynman diagrams are shown in Fig. 5(b-d) with self-energy part $\chi_J^{(1,bc)}$ in Fig. 5(b,c) and vertex part $\chi_J^{(1,d)}$ in Fig. 5(d). The analytic expressions of these contributions read

$$\chi_J^{(1,bc)}(i\omega) = -T^2\sum_{\boldsymbol{k}\epsilon\epsilon'\nu}\int\frac{d^2q}{(2\pi)^2}V(\boldsymbol{q})\mathrm{Tr}\big(J_{\boldsymbol{k}\nu}G_{\boldsymbol{k},i\omega+i\epsilon}J_{\boldsymbol{k}\nu}G_{\boldsymbol{k},i\epsilon}M_{\boldsymbol{q}}G_{\boldsymbol{k}+\boldsymbol{q},i\epsilon'}M_{-\boldsymbol{q}}G_{\boldsymbol{k},i\epsilon}\big) \tag{31}$$

$$\chi_J^{(1,d)}(i\omega) = \frac{T^2}{2}\sum_{\boldsymbol{k}\epsilon\epsilon'\nu}\int\frac{d^2q}{(2\pi)^2}V(\boldsymbol{q})\mathrm{Tr}\big(J_{\boldsymbol{k}\nu}G_{\boldsymbol{k},i\omega+i\epsilon}M_{\boldsymbol{q}}G_{\boldsymbol{k}+\boldsymbol{q},i\omega+i\epsilon'}J_{\boldsymbol{k}\nu}G_{\boldsymbol{k}+\boldsymbol{q},i\epsilon'}M_{-\boldsymbol{q}}G_{\boldsymbol{k},i\epsilon}\big). \tag{32}$$

Here, $G_{\boldsymbol{k},i\omega}$ denotes the bare Green's function, see Eq. (6), and the matrix $M_{\boldsymbol{q}}$, see Eq. (16), accounts for the spatial separation of the two carbon basis atoms. Like in case of the self-energy discussed in Sec. II C, it plays an important role in the following evaluation of $\chi_J^{(1)}$ as it renders the integration over momentum $\boldsymbol{q}$ finite.

To obtain $\chi_J^{(1,bc)}$, we insert the result for the self-energy $\Sigma(\boldsymbol{k})$ into Eq. (31). The self-energy is obtained by summing over 4.6×10^4 Bravais lattice vectors using Eq. (25). As shown in detail in Appendix A 2 and A 3, we then first analytically continue $i\omega \to \omega + i\delta$, before evaluating the remaining momentum summation over the first Brillouin zone. By first performing the analytic continuation, the momentum summation turns into a one-dimensional integration along a contour around the two Dirac nodes (in case of small external frequency ω), which can be efficiently computed numerically.

The vertex contribution $\chi_J^{(1,d)}$ in Eq. (32) is evaluated in a similar way and we refer to Appendix A 3 and A 4 for details. The presence of the matrix $M_{\boldsymbol{q}}$ inside the trace again ensures convergence of the $\boldsymbol{q}$-integration.

As shown in Fig. 7, the individual contributions $\sigma^{(1,j)}$ of self-energy and vertex diagrams to the optical conductivity correction

$$\sigma^{(1)} = \sigma_0\alpha\mathcal{C} = \sigma^{(1,bc)} + \sigma^{(1,d)} = \sigma_0\alpha(\mathcal{C}_{bc} + \mathcal{C}_d) \tag{33}$$

diverge logarithmically in the low frequency limit ω/D, where $D = 6t$ is the bandwidth. Their sum, however, remains finite and, as shown in Fig. 2, yields (within numerical accuracy) the coefficient $\mathcal{C}$ with the numerical value $(19-6\pi)/12$ given in Eq. (2). The inset of Fig. 2 shows that $\sigma^{(1)}$ is independent of the ratio λ/a, demonstrating the universal nature of the optical conductivity of graphene.

To compare with experiment, we use our result of the optical conductivity $\sigma(\omega)$ to calculate the optical transparency of graphene $T(\omega)$. In Fig. 8, we compare experimental results for $T(\lambda)$, where $\lambda = 2\pi c/\omega$, reported by Nair *et al.* in Ref. 25 with different theoretical approaches of computing $\sigma(\omega)$, both using the Dirac approximation and using the full tight-binding (nearest-neighbor) lattice theory. We observe that in the optical range, the main correction to the non-interacting Dirac approximation result σ_0(Dirac) stems from the non-linearity of the band structure, i.e., from deviations from the linear dispersion in the tight-binding band structure of graphene. The additional interaction corrections are minute, because the coefficient $\mathcal{C}$ is incidentally quite small. Note that a larger coefficient such as $\mathcal{C}'$ implies a much more pronounced shift of the transparency from the non-interacting result (which is not observed experimentally).

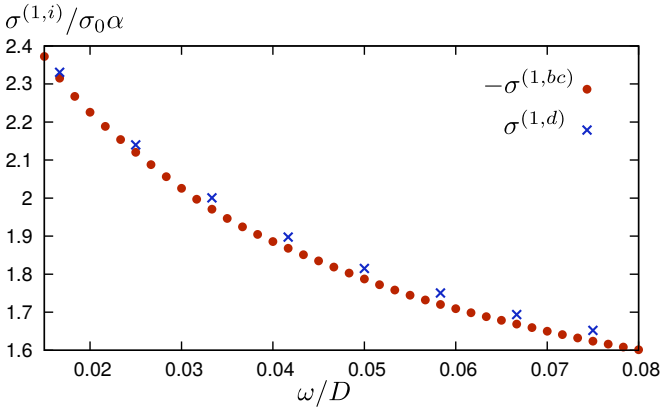

FIG. 7. (Color online) Plot of the self-energy σ_{bc} and vertex-correction σ_d contributions to the frequency-dependent conductivity, normalized to $\sigma_0\alpha$ (see Eq. (33)). The separate contributions diverge in the low-frequency limit $\omega \ll D$.

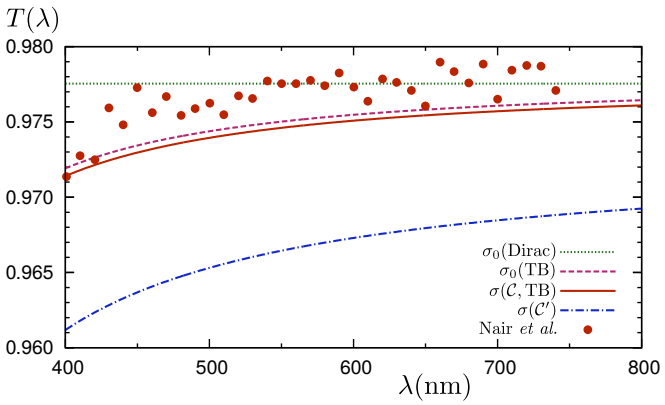

FIG. 8. (Color online) Optical transmission through graphene as function of wavelength λ. Comparison of experimental results (red dots) from Ref. 25 and theory: non-interacting Dirac fermions σ_0(Dirac) and tight-binding theory $\sigma_0(\omega, \mathrm{TB})$; interacting tight-binding prediction $\sigma(\mathcal{C}, \mathrm{TB}) = \sigma_0(\omega, \mathrm{TB})[1+\mathcal{C}\alpha(\omega)]$, and $\sigma(\mathcal{C}') = \sigma_0(\omega, \mathrm{TB})[1 + \mathcal{C}'\alpha(\omega)]$. Note that $\sigma_0(\omega, \mathrm{TB})$ deviates from σ_0(Dirac) for higher frequencies more strongly than previously reported in Refs. 25 and 30.

How does our numerical result of $\mathcal{C}$ given in Eq.(2) compare with Ref. 20, who claim to have performed an evaluation of the conductivity of the tight-binding model, but find the larger value $\mathcal{C}'$? Following the details of Ref. 20 included in the supplementary material of that paper one finds that, in the end, the authors do not evaluate the conductivity numerically, but perform a nodal approximation and regularize divergent integrals in a fashion that violates charge conservation. The final expression of the conductivity coefficient of Ref. 20 is not the correct lattice version of the conductivity anyway, as Eq. (15) of that work lacks the distinction between BZ restricted and unrestricted momentum integrations, discussed above.

III. FIELD THEORETICAL APPROACH IN THE DIRAC LIMIT

Within the Dirac theory of graphene, both self-energy and vertex contributions to the interaction correction of the conductivity, $\sigma^{(1,bc)}$ and $\sigma^{(1,d)}$, involve divergent integrals as, e.g., the momentum cutoff is sent to $\Lambda \to \infty$ or the physical dimensionality is restored $\epsilon \to 0$. The main goal in this section is to reconcile the results of dimensional regularization as presented in the detailed calculations of Juricic, Vafek and Herbut (JVH) in Ref. 19 with the tight-binding results of Sec. II. The authors of Ref. 19 regularize the divergent integrals appearing in the calculation of $\sigma^{(1,j)}$ $(j = bc, d)$ by working in $d = 2 - \epsilon$ dimensions, add both contributions and take the limit $\epsilon \to 0$ in the end.

An alternative scheme to perform dimensional regularization was presented by Teber and Kotikov (TK) in Ref. 33. It is based on the modified minimal subtraction $\overline{\mathrm{MS}}$ scheme,[36] and the corresponding continuum renormalization group (RG). In Sec. III A, we describe the $\overline{\mathrm{MS}}$ calculation in detail and confirm the TK results. As found by TK, although adding the interaction correction diagrams b, c and d yields the numerical result $\mathcal{C}'$ for the correction coefficient, one must consider that within the $\overline{\mathrm{MS}}$ scheme of dimensional regularization, the bare bubble contribution is also renormalized. This gives an additional contribution that finally yields the numerical result $\mathcal{C}$ for the interaction correction coefficient (see Eq. (2)), in agreement with the lattice theory of Sec. II.

In Sec. III B, we add to the insight of TK by examining the conductivity scaling relation in $d = 2 - \epsilon$ dimensions,[37] which relates the true conductivity (left side) to the renormalized one (right side):

$$\sigma(\omega, \alpha) = \lim_{\Lambda\to\infty} \lim_{\epsilon\to 0} b^{\epsilon}\sigma\big(\omega/Z_T, \alpha(b), \Lambda\big)\,. \tag{34}$$

Here, $b > 1$ is a scaling factor, Z_T is the renormalization factor of the frequency equal to $Z_T(b) = [4\epsilon + \alpha(b^{\epsilon} - 1)]/4\epsilon b$ and the running coupling constant reads $\alpha(b) = 4\epsilon\alpha b^{\epsilon}/[4\epsilon + \alpha(b^{\epsilon} - 1)]$.[29] We compute the conductivity of graphene in $d = 2 - \epsilon$ dimensions, but including an ultraviolet (UV) momentum cutoff Λ. Importantly, we show that the limits of $\epsilon \to 0$ and $\Lambda \to \infty$ do not commute, a phenomenon that we refer to as UV quirk.

If one furthermore employs the relation between the conductivity and density-density correlator χ_ρ used in the original work of Mishchenko,[17] it is possible to precisely isolate the origin of the UV quirk as coming from the self-energy (bc) diagrams. We show that, if one maintains a UV cutoff in d dimensions (as implied by the Wilson momentum shell RG), the result $\mathcal{C}$ is obtained when the limit $d \to 2$ is taken. In contrast, if one works in $d = 2 - \epsilon$ dimensions but with $\Lambda \to \infty$, the self-energy (bc) diagrams yield a different result, leading to the coefficient $\mathcal{C}'$. Importantly however, in this case of $\Lambda \to \infty$, the theory must be regularized using the $\overline{\mathrm{MS}}$ scheme, which yields the numerical values $\mathcal{C}$ in Eq. (2) for the interac-

tion correction coefficient (see Sec. III A), in agreement with the lattice calculation.

A. Continuum renormalization group and modified minimal subtraction $\overline{\text{MS}}$ scheme

In this section, we largely follow the work of Teber and Kotikov (TK) in Ref. 33, in particular highlighting the differences between the dimensional regularization using the modified minimal subtraction $\overline{\text{MS}}$ scheme compared to the Wilson momentum shell RG. When using dimensional regularization, we do not introduce an UV-cutoff Λ to our system. The system is regularized by the dimensionless parameter ϵ. As reported by JVH and TK (and confirmed by us), dimensional regularization of the interaction-dependent diagrams leads to a result implying that the correction coefficient is $\mathcal{C}' = \frac{22-6\pi}{12}$.[19,33] However, as found by TK, the whole theory is divergent and needs to be regularized by the continuum renormalization group. This is done by introducing counterterms that remove these divergences. After this renormalization procedure, it is found that the bare-bubble contribution is *also* modified, finally yielding the correction coefficient $\mathcal{C} = \frac{19-6\pi}{12}$.

Our starting point is the action of graphene

$$S = \int d\tau \int d^d x \; \psi_0^\dagger \left(\partial_\tau + i e_0 A_0^0 + v_0(-i\boldsymbol{\nabla}\boldsymbol{\sigma})\right) \psi_0 + \int d\tau \int d^{d_\gamma} x \left(\partial_x A_0^0\right)^2 , \tag{35}$$

where $d = 2-\epsilon$ is the spatial dimensionality of the electronic degrees of freedom and $d_\gamma = 3$ that of the gauge fields A_0. The subscript "0" denotes bare quantities: the fermionic field ψ_0 and the gauge field A_0, which mediates the Coulomb interaction with potential

$$V(\mathbf{q}) = \frac{2\pi e^2}{|\boldsymbol{q}|} \frac{r_0^{-\epsilon}\pi^{-\epsilon/2}\Gamma\left(\frac{1}{2}\right)}{\Gamma\left(\frac{1-\epsilon}{2}\right)} . \tag{36}$$

The length scale r_0 is introduced in such a way, that the Coulomb potential has the correct units in $d = 2-\epsilon$. From this action one can derive physical observables which are divergent in the limit $\epsilon \to 0$. One of these divergent physical observables is the self-energy

$$\Sigma(q) = \Phi(q) v_0 \mathbf{q}\cdot\boldsymbol{\sigma} = \alpha_0 \frac{2^{2\epsilon-3}\Gamma\left(\frac{\epsilon}{2}\right)}{\Gamma\left(1-\frac{\epsilon}{2}\right)} (r_0 q)^{-\epsilon} v_0 \mathbf{q}\cdot\boldsymbol{\sigma} . \tag{37}$$

Note that the self-energy is proportional to $1/\epsilon$, which follows from expanding the function $\Phi(p)$ for small ϵ

$$\Phi(p) \approx \frac{\alpha_0}{4}\frac{1}{\epsilon} + \frac{\alpha_0}{4}\left[\log(4) - \log(p r_0) - \gamma\right] + \mathcal{O}(\epsilon) . \tag{38}$$

Here, we explicitly see that the theory has divergences. In order to render it finite, we introduce renormalized (physical) fields, which we denote with a subscript "R":

$$\psi_0 = \sqrt{Z_\psi}\psi_R, \tag{39}$$
$$A_0 = \sqrt{Z_A} A_R, \tag{40}$$
$$v_0 = Z_v v_R, \tag{41}$$
$$e_0 = \frac{Z_1}{Z_\psi\sqrt{Z_A}} e_R = Z_e e_R , \tag{42}$$

which leads to the following renormalized Lagrangian density

$$\mathcal{L}_R = Z_\psi \; \psi_R^\dagger \partial_\tau \psi_R + i e_0 \sqrt{Z_A} Z_\psi \; \psi_R^\dagger A_R^0 \psi_R + Z_v Z_\psi \; v_R \psi_R^\dagger (-i\boldsymbol{\nabla}\cdot\boldsymbol{\sigma})\psi_R + Z_A \; \left(\partial_x A_R^0\right)^2 . \tag{43}$$

To obtain a finite theory, we introduce counterterms via $Z_\psi = 1+\delta_\psi$, $Z_A = 1+\delta_A$, $Z_v = 1+\delta_v$ and $Z_e = 1+\delta_e$ These counterterms are chosen in such a way as to cancel the divergences. In the case of the self-energy, we find

$$\Sigma(q) = \Phi_R(q) v_R \mathbf{q}\cdot\boldsymbol{\sigma} + \delta_v v_R \mathbf{q}\cdot\boldsymbol{\sigma} + \delta_\psi \left(i\Omega + v_R \mathbf{q}\cdot\boldsymbol{\sigma}\right) . \tag{44}$$

From Eq. (38) we know that the divergence of the self-energy is independent of frequency, and thus $\delta_\psi = 0$ and therefore $Z_\psi = 1$. The velocity counterterm, on the other hand, must cancel the divergence of the self-energy, demanding

$$\delta_v = -\frac{\alpha_R}{4}\frac{1}{\epsilon} \;\Rightarrow\; Z_v = \left(1 - \frac{\alpha_R}{4\epsilon}\right) . \tag{45}$$

The electric charge e remains unrenormalized in graphene, i.e. $Z_e = 1$.

Next, we will use the modified minimal subtraction $\overline{\text{MS}}$ scheme, where one introduces a physical energy scale μ in such a way that the physical observables become dimensionless and the divergence is removed.[36] In other words, we substitute the divergence $1/\epsilon$ by a logarithm depending on the physical scale μ:

$$\frac{1}{\epsilon} \to \log\left(\mu/\omega\right) . \tag{46}$$

Using this substitution, the slope of the self-energy becomes

$$\Phi_R(p) = \frac{\alpha_R}{4}\frac{1}{\epsilon} + \frac{\alpha_R}{4}\ln\left(\frac{4e^{-\gamma}}{p r_0}\right) = -\frac{\alpha_R}{4}\ln\left(\frac{p r_0}{\tilde{\mu}/\omega}\right) , \tag{47}$$

with $\tilde{\mu} = 4e^{-\gamma}\mu$. As shown in detail in Appendix B, the same procedure yields for the coupling constant α and the velocity v the non-divergent observables

$$\alpha(\mu) = \frac{\alpha_0 4^\epsilon e^{-2\gamma\epsilon}\tilde{\mu}^{-2\epsilon}}{1+\frac{\alpha_0}{4}\frac{1}{\epsilon}4^\epsilon e^{-2\gamma\epsilon}\tilde{\mu}^{-2\epsilon}} \to \alpha(\mu) = \frac{\alpha_0}{1+\frac{\alpha_0}{4}\log\left(\frac{\mu}{\omega}\right)} \tag{48}$$

$$v(\mu) = v_0 + \frac{e_0^2}{4\epsilon}4^\epsilon e^{-2\gamma\epsilon}\tilde{\mu}^{-2\epsilon} \to v(\mu) = v_0 + \frac{e_0^2}{4}\log\left(\frac{\mu}{\omega}\right) . \tag{49}$$

Finally, the bare non-interacting optical conductivity σ_0, which requires calculating the bare-bubble diagram in spatial dimension $d = 2-\epsilon$, is given by

$$\sigma_{0,0}(\omega) = e_0^2 N A_\epsilon \left|\frac{v_0}{\omega}\right|^\epsilon , \tag{50}$$

with

$$A_\epsilon = 4^{-2+\epsilon}\pi^{\epsilon/2}\frac{(1-\epsilon)}{\Gamma\left(1-\frac{\epsilon}{2}\right)} . \tag{51}$$

To remove all divergences in the theory, we have to replace all bare quantities such as the charge e_0 and the velocity v_0 by their renormalized values, which yields

$$\sigma_{0,R}(\omega) = \frac{e^2(\mu)}{4^\epsilon}e^{2\gamma\epsilon}\tilde{\mu}^{2\epsilon}NA_\epsilon\left|\frac{\left(1-\frac{\alpha(\mu)}{4\epsilon}\right)v_R}{\omega}\right|^\epsilon , \tag{52}$$

where $e^2(\mu) = 4^\epsilon e_0^2 e^{-2\gamma\epsilon}\tilde{\mu}^{-2\epsilon}$ (for details see Appendix B). According to equation (48), one can choose $\alpha(\mu)$ such that it is a small quantity, reflecting that α is marginally irrelevant at the upper critical dimension $d = 2$. We can thus approximate[33]

$$\left(1-\frac{\alpha(\mu)}{4\epsilon}\right)^\epsilon \approx 1-\frac{\alpha(\mu)}{4} . \tag{53}$$

Inserting this into our expression for the non-interacting conductivity and taking the limit $\epsilon \to 0$, we obtain

$$\sigma_0(\omega) \equiv \sigma_{0,R}(\omega) = \sigma_0\left(1-\frac{\alpha(\omega)}{4}\right) , \tag{54}$$

where $\sigma_0 = e_0^2 N/16$. Importantly, the bare-bubble result is modified due to the velocity renormalization. Remarkably, as found by TK, this term combines with the $\mathcal{O}(\alpha)$ vertex and self-energy diagrams in Fig. 5(b-d), which yield, within dimensional regularization in $d = 2-\epsilon$ dimensions, an interaction correction coefficient[19,33]

$$\mathcal{C}' = \frac{22-6\pi}{12} , \tag{55}$$

Although this apparently leads to a result that disagrees with other regularization schemes, regularizing the full theory (via counterterms) leads to the additional contribution in Eq. (54), which must be included. Summing all terms to order α finally yields

$$\sigma(\omega) = \sigma_0\Big(1+\mathcal{C}'\alpha(\omega)-\frac{\alpha(\omega)}{4}\Big) = \sigma_0\big(1+\mathcal{C}\alpha(\omega)\big) , \tag{56}$$

The final interaction correction coefficient therefore takes the value in Eq. (2):

$$\mathcal{C} = \frac{19-6\pi}{12} , \tag{57}$$

in agreement with the lattice calculation of Sec. II.

B. Wilson momentum shell RG combined with dimensional regularization

In this section we show that combining the Wilson momentum shell RG (WRG) with dimensional regularization (DR) yields an ultraviolet (UV) quirk as the physical dimension $d = 2$ of graphene is restored at the end of the calculation. Specifically, we demonstrate that the order of limits of sending the UV cutoff Λ to infinity and the parameter ϵ, introduced by DR in $d = 2-\epsilon$ dimensions, to zero does not commute. In practice, this means that the additional renormalization factor appearing in the bare bubble term of the TK calculation (see Eq. (54)) is not present when we use the WRG in $d = 2-\epsilon$ dimensions. This factor only occurs in the absence of any cutoff (pure DR), when counterterms are required to regularize the theory. As shown in the previous section III A, in this case the counterterm $\mathcal{O}(\alpha)$ contribution of the non-interacting conductivity combines with the coefficient $\mathcal{C}'$ arising from the leading order self-energy and vertex interaction correction diagrams to, again, yield the correction coefficient $\mathcal{C}$. In contrast, the WRG approach in d dimensions directly obtains $\mathcal{C}$ without the factor in Eq. (54), as long as Λ is sent to ∞ only at the end of the calculation, i.e. in particular after $\epsilon \to 0$.

In the following, in Sec. III B 1, we first review in strictly $d = 2$ the approach by Mishchenko from Ref. 17 of using the density-density correlator $\chi_\rho(\boldsymbol{q},\omega)$ to obtain the optical conductivity via

$$\sigma(\omega) = \lim_{|q|\to 0}\frac{\omega}{|\boldsymbol{q}|^2}\mathrm{Im}\chi_\rho(\boldsymbol{q},\omega) . \tag{58}$$

Then, in Sec. III B 2, we discuss how this calculation changes if the integrals are regularized by changing the dimension to $d = 2-\epsilon$ instead of using a momentum cutoff. Finally, in Sec. III B 3 we show the appearance of an UV quirk by keeping a momentum cutoff in $d = 2-\epsilon$ dimensions. We demonstrate that the two limits $\Lambda \to \infty$ and $\epsilon \to 0$ do not commute and that the correct order of limits, which is sending $\epsilon \to 0$ before $\Lambda \to \infty$ as demanded by the WRG, yields the results $\mathcal{C}$ in agreement with the lattice calculation.

1. *Conductivity via Mishchenko's approach in $d = 2$ and with momentum cutoff Λ*

Let us evaluate the conductivity following Mishchenko's approach of using the density-density correlator.[17] We work in $d = 2$ dimensions and keep a

momentum cutoff Λ in the Coulomb interaction potential. Within this approach, divergences only appear in the self-energy diagrams (similar to Fig. 5(b,c)). This makes it easier to see the impact of the regularization scheme, i.e. momentum cutoff versus dimensional regularization, which is discussed in the next Sec. III B 2.

Within Mishchenko's approach, the conductivity is obtained via Eq. (58), where χ_ρ is the retarded density-density correlator. To obtain the self-energy contributions to Eq. (58) (see Fig. 5(b) and (c)) , we need to compute the self-energy that we have previously shown to be given by[18]

$$\Sigma(\boldsymbol{k}) = -\int \frac{d^2q}{(2\pi)^2}\int \frac{d\epsilon}{2\pi} V(\boldsymbol{k}-\boldsymbol{q}) G_{\boldsymbol{q},i\epsilon} = \frac{1}{4}\alpha v \boldsymbol{k}\cdot\boldsymbol{\sigma}\ln\Big(\frac{4\Lambda\sqrt{e}}{p}\Big), \tag{59}$$

where $V(\boldsymbol{q}) = \frac{2\pi e^2}{|\boldsymbol{q}|}\theta(\Lambda - |\boldsymbol{q}|)$ contains the momentum cutoff Λ. With this result, the contribution due to the self-energy type diagrams is (note we multiplied by 2 for the two diagrams and set $v = 1$ for brevity):

$$\chi_\rho^{(1,bc)}(\boldsymbol{q},\omega) = -\frac{1}{2}Ne^2\alpha\int\frac{d^2p}{(2\pi)^2}\int\frac{d\epsilon}{2\pi}\ln\frac{4\Lambda\sqrt{e}}{p}\mathrm{Tr}\Big(\frac{-i\epsilon\sigma_0 - \boldsymbol{p}\cdot\boldsymbol{\sigma}}{\epsilon^2+p^2}\frac{-i(\epsilon+\omega)\sigma_0 - (\boldsymbol{p}+\boldsymbol{q})\cdot\boldsymbol{\sigma}}{(\epsilon+\omega)^2+(\boldsymbol{p}+\boldsymbol{q})^2}\frac{-i\epsilon\sigma_0 - \boldsymbol{p}\cdot\boldsymbol{\sigma}}{\epsilon^2+p^2}\boldsymbol{p}\cdot\boldsymbol{\sigma}\Big). \tag{60}$$

Evaluating the trace yields

$$\chi_\rho^{(1,bc)}(\boldsymbol{q},\omega) = -\frac{1}{2}Ne^2\alpha\int\frac{d^2p}{(2\pi)^2}\int\frac{d\epsilon}{2\pi}\ln\frac{4\Lambda\sqrt{e}}{p}\frac{-2}{(\epsilon^2+p^2)^2}\frac{p^4 - 3\epsilon^2p^2 - 2\epsilon\omega p^2 - \boldsymbol{q}\cdot\boldsymbol{p}(\epsilon^2-p^2)}{(\epsilon+\omega)^2+(\boldsymbol{p}+\boldsymbol{q})^2}. \tag{61}$$

Expanding to quadratic order in q and integrating over angles gives (keeping only the q^2 term)

$$\chi_\rho^{(1,bc)}(\boldsymbol{q},\omega) = -\frac{1}{2}Ne^2\alpha\frac{q^2}{8\pi^3}\int_0^\infty pdp\int_{-\infty}^\infty d\epsilon\ln\frac{4\Lambda\sqrt{e}}{p}\frac{8p^2\pi}{(\epsilon^2+p^2)^2}\frac{(\omega+\epsilon)(\omega+2\epsilon)[p^2-\epsilon(\omega+\epsilon)]}{[p^2+(\epsilon+\omega)^2]^3}. \tag{62}$$

To proceed, we restore the velocity v and introduce the dimensionless variable $\tilde{p} = vp/\omega$. Evaluating the frequency integral results in

$$\chi_\rho^{(1,bc)}(\boldsymbol{q},\omega) = -\frac{1}{2}Ne^2\alpha\frac{q^2}{8\pi^3}\frac{1}{\omega}\int_0^\infty d\tilde{p}\tilde{p}\ln\frac{v\Lambda\sqrt{e}}{\tilde{p}\omega}\frac{\pi^2(4\tilde{p}^2-1)}{\tilde{p}(4\tilde{p}^2+1)^2} = \frac{N\alpha}{64}\frac{q^2}{\omega}. \tag{63}$$

Note that the integral over $\tilde{p}$ was a sum of two terms due to the formula

$$\ln\frac{v\Lambda\sqrt{e}}{\tilde{p}\omega} = \ln\frac{v\Lambda\sqrt{e}}{\omega} - \ln\tilde{p}. \tag{64}$$

However, the first integral containing the factor $\ln(v\Lambda\sqrt{e}/\omega)$ *vanishes*. Thus, despite a divergent self-energy, resulting in the cutoff dependence of the integrand, the corresponding contribution to the conductivity is not divergent and independent of Λ. Upon analytic continuation, we find the contribution to the conductivity

$$\sigma^{(1,bc)} = \sigma_0\frac{\alpha}{4}, \tag{65}$$

or $\sigma_{bc} \equiv \sigma^{(1,bc)}/\sigma_0\alpha = 1/4$. This agrees with Eq.(13) in Ref. 17 by Mishchenko.

As we have noted, within this approach, the vertex (d) diagram (see Fig. 5(d)) contains no divergences and is given by

$$\sigma^{(1,d)} = \sigma_0\alpha\frac{8-3\pi}{6}, \tag{66}$$

or $\sigma_d = (8-3\pi)/6$. This finally leads to

$$\sigma = \sigma_0\Big(1+\alpha\frac{19-6\pi}{12}\Big), \tag{67}$$

in agreement with the lattice calculation. Next, we discuss how dimensional regularization can give a different result via the appearance of an UV quirk.

2. *Dimensional regularization without momentum cutoff*

We now consider how the results of the last section change if one works in $d = 2-\epsilon$ dimensions to regularize the integral instead of using a momentum cutoff Λ, i.e. sending $\Lambda\to\infty$. The limit $\epsilon\to 0$ is performed at the end of the calculation. In this case, we find a result that is obtained by simply replacing the logarithm in the self-energy in Eq. (59)) with the self-energy derived from dimensional regularization and altering the dimensionality of the momentum integral. We find that the self-energy in d dimensions is proportional to[19]

$$\Sigma(p) \propto p^{-\epsilon}\frac{\Gamma\left[\frac{1-\epsilon}{2}\right]\Gamma\left[\frac{3-\epsilon}{2}\right]\Gamma\left[\frac{\epsilon}{2}\right]}{\pi\Gamma[2-\epsilon]}$$

$$= \frac{1}{\epsilon} - \frac{1}{2}\gamma + \ln 4 - \ln p + \mathcal{O}(\epsilon)\,. \tag{68}$$

As noted above, when calculating χ_ρ one performs an integration over momentum $\boldsymbol{p}$ (see Eq. (63)) and only the $\ln p$ part of Eq. (68) contributes. Given this fact, one may ask how a different result can arise in dimensional regularization compared to regularization by a momentum cutoff Λ, since the only change is the replacement $\ln\Lambda \to \frac{1}{\epsilon}$ (up to additional constant terms). In strictly two dimensions, but with the self-energy evaluated in $d = 2-\epsilon$ dimensions (to regularize), one finds for the dimensionless integral (see Eq. (63))

$$I_{d=2,\Lambda=\infty} \equiv \chi_\rho^{(1,bc)} \frac{16\pi^3\omega}{Ne^2\alpha q^2} = \int_0^\infty d\tilde{p}\tilde{p}\Big[\frac{1}{\epsilon} - \frac{1}{2}\gamma + \ln\frac{4}{\tilde{p}}\Big]\frac{4\tilde{p}^2-1}{\tilde{p}(4\tilde{p}^2+1)^2} = \int_0^\infty \tilde{p}d\tilde{p}\ln\frac{1}{\tilde{p}}\frac{4\tilde{p}^2-1}{\tilde{p}(4\tilde{p}^2+1)^2} = -\frac{\pi}{4}\,. \tag{69}$$

where we have used that the integral over the momentum-independent piece in square brackets vanishes. The subscript of $I_{d=2,\Lambda=\infty}$ refers to the dimensionality of the p-momentum integral d in Eq. (69) and to the momentum cutoff Λ used in the evaluation of the self-energy in $(2-\epsilon)$ dimensions. In Eq. (69) we used the expression for the self-energy in Eq. (68), which is evaluated in $(2-\epsilon)$ dimensions with a momentum cutoff sent to infinity. Clearly, $I_{d=2,\Lambda=\infty} = -\pi/4$ would yield the result in Eq. (67) whether the cutoff comes from Λ or from dimensional regularization. However, in d dimensions, the integration measure of the p-momentum integral also changes, and one instead of Eq. (69) one rather needs to consider $I_{d=2-\epsilon,\Lambda=\infty}$, which reads

$$\begin{aligned} I_{2-\epsilon,\infty} &= \int_0^\infty d\tilde{p}\tilde{p}^{1-\epsilon}\Big(\frac{1}{\epsilon} - \frac{1}{2}\gamma + \ln\frac{4}{\tilde{p}}\Big)\frac{4\tilde{p}^2-1}{\tilde{p}(4\tilde{p}^2+1)^2} \\ &= -\frac{\pi}{2}, \end{aligned} \tag{70}$$

where we took $\epsilon \to 0$ at the end of the calculation. Importantly, in Eq. (70), the part of the integral coming from the momentum-independent parts of the square bracket does not vanish. Instead, it is proportional to ϵ and yields a finite contribution when multiplied by $1/\epsilon$. This difference doubles the size of the self-energy (bc) diagrams, from $\pi/4$ in Eq. (69) to $\pi/2$ in Eq. (70).

Since the vertex diagram does not change, because it is convergent, this would lead to the final conductivity correction proportional to the coefficient $\mathcal{C}' = (22-6\pi)/12$, as reported by JVH.[19] In the next Sec. III B 3, we show, however, that this conclusion is erroneous as it does not correctly take into account that the Wilsonian momentum shell RG implicitly requires a finite momentum cutoff Λ, even in $d = 2-\epsilon$ dimensions. Note that in Eq. (70), we approximated the self-energy by its Taylor series expression up to order $\mathcal{O}(\epsilon^0)$, but the same result is obtained if one instead uses the full power-law expression of Eq. (68).

3. *Spatial dimension $d = 2-\epsilon$ but sharp cutoff*

Let us now consider a calculation in $d = 2-\epsilon$ dimensions that still keeps a momentum cutoff Λ. This is motivated by the observation that when performing a Wilson momentum shell RG in d dimensions, one implicitly keeps a cutoff Λ around which momentum shells are integrated out. While we need a cutoff Λ once we restore the physical dimension $d = 2$, we naively expect it to play no role once we work in $d = 2-\epsilon$ dimensions, since all momentum integrations are finite for $\epsilon > 0$. Nevertheless, as we now show, here an UV quirk appears once we consider the limits $\epsilon \to 0$ and $\Lambda \to \infty$, which turn out to not commute. In $d = 2-\epsilon$ dimensions and maintaining a UV cutoff Λ, the self-energy is of the form

$$\Sigma(p) \propto \int_p^\Lambda \frac{q^{d-1}dq}{q^2} = \frac{1}{\epsilon}\Big(p^{-\epsilon} - \Lambda^{-\epsilon}\Big). \tag{71}$$

Plugging this into the integral for $\chi_\rho^{(1,bc)}$ in Eq. (63), we obtain

$$\int_0^\infty dpp^{1-\epsilon}\frac{1}{\epsilon}\Big(p^{-\epsilon} - \Lambda^{-\epsilon}\Big)\frac{4(vp)^2-\omega^2}{p(4(vp)^2+\omega^2)^2} = \Big(\frac{\omega}{v}\Big)^{1-2\epsilon}\frac{\frac{\pi}{4}\left(\frac{\omega}{v\Lambda}\right)^\epsilon - \frac{\pi}{2}}{\omega^2}\,. \tag{72}$$

which reveals the UV quirk: the order of limits of sending the UV cutoff $\Lambda \to \infty$ and the dimensional parameter $\epsilon \to 0$ do not commute. As a result, the numerical value of the interaction correction coefficient

$$C\Big(\epsilon, \frac{\omega}{\Lambda}\Big) = \frac{22 - 6\pi - 3\Big(\frac{\omega}{v\Lambda}\Big)^\epsilon}{12} \tag{73}$$

is affected by the order of limits. If we first take the limit of $\epsilon \to 0$ before $\Lambda \to \infty$, we obtain $\mathcal{C}$. However, if we instead take $\Lambda \to \infty$ first before $\epsilon \to 0$, we obtain $\mathcal{C}'$, i.e.,

$$\lim_{\epsilon\to 0}\Big(\lim_{\Lambda\to\infty} C\Big(\epsilon, \frac{\omega}{\Lambda}\Big)\Big) = \mathcal{C}' \tag{74}$$

$$\lim_{\Lambda\to\infty}\Big(\lim_{\epsilon\to 0} C\Big(\epsilon, \frac{\omega}{\Lambda}\Big)\Big) = \mathcal{C}\,. \tag{75}$$

Within Wilson momentum shell RG, the solution to this ultraviolet quirk is to always maintain a nonzero cutoff Λ, first setting $\epsilon \to 0$. As shown in Eq. (75), this procedure unambiguously yields the coefficient $\mathcal{C}$. If we instead wish to set $\Lambda \to \infty$ first then, although the theory is regularized, additional singularities appear in the limit $\epsilon \to 0$. A correct handling of this limit requires regularizing the full theory (not just the self-energy and vertex diagrams) using, for example, the minimal subtraction scheme reviewed in the preceding subsection. This procedure then again yields the numerical value $\mathcal{C}$ for the interaction correction coefficient, in agreement with our lattice calculation in Sec. II.

IV. CONCLUSION

In conclusion, we have evaluated the optical conductivity $\sigma(\omega)$ of graphene including the lowest order Coulomb interaction corrections within a full lattice tight-binding approach. In the non-interacting limit, we correct previous results of the conductivity $\sigma_0(\omega)$ beyond the Dirac limit σ_0. Considering interactions, within our lattice calculation we explicitly show that $\sigma(\omega)$ is universal and independent of other dimensionless quantities such as the ratio of the width of the atomic orbitals λ to the lattice constant a (in the frequency regime $\omega < v\Lambda$).

Equipped with this insight, we address in the second part of our work, a controversy of how to obtain the correct result for $\sigma(\omega)$ within a Dirac low-energy description of graphene, where only the linear part of the spectrum is taken into account. Such a theory needs to be regularized and, as previously reported, different regularization schemes apparently yield different results. Here, we resolve this issue by demonstrating the appearance of an ultraviolet quirk when dimensional regularization is combined with the momentum shell renormalization group. In this situation, the order of limits of sending the dimensionality to the physical dimension and the momentum cutoff to infinity do not commute. We point out the correct order of limits and show that this results in a final result in agreement with our lattice calculation.

Our work thus validates previous Dirac approximation calculations, and resolves a long-standing controversy about the correct way to regularize the Dirac theory showing clearly why previous incorrect approaches failed. Since descriptions of electronic systems by effective low-energy models like the Dirac Hamiltonian of graphene are the cornerstone of condensed matter physics, it is gratifying that our work confirms the quantitative accuracy of this method.

A practical implication of this insight is that dimensional regularizations with $d = 2 - \epsilon$ for the fermionic degrees of freedom are full of subtleties. If one wants to investigate the role of Coulomb interactions in graphene and wishes to avoid a regularization via an explicit cut off, it is technically easier to perform this regularization with regards to the embedding space of the photon field $d_\gamma = 2 - \eta$. This approach was performed in Ref. 18 and immediately yields the correct result and no oder of limit issues occur.

V. ACKNOWLEDGEMENTS

We gratefully acknowledge useful discussions with U. Briskot, I. Herbut, A. Mirlin, E. Mishchenko, C. Seiler, S. Teber and O. Vafek. J.M.L. acknowledges the hospitality of the Department of Physics and Astronomy at Louisiana State University, where part of this work was carried out, as well as financial support from the US National Science Foundation and the Carl-Zeiss-Stiftung. The Young Investigator Group of P.P.O. received financial support from the "Concept for the Future" of the Karlsruhe Institute of Technology (KIT) within the framework of the German Excellence Initiative. D.E.S. was supported by the National Science Foundation Grant No. DMR-1151717 and by the German Academic Exchange Service (DAAD). This work was performed on the computational resource bwUniCluster funded by the Ministry of Science, Research and the Arts Baden-Württemberg and the Universities of the State of Baden-Württemberg, Germany, within the framework program bwHPC.

Note added.– After submission of this manuscript, a quantum Monte-Carlo analysis appeared[38] with results that are consistent with ours.

Appendix A: Perturbative calculation of the conductivity

The frequency-dependent conductivity follows from the Kubo formula, which we now briefly review.[34] Using the Peierls substitution to couple an electromagnetic gauge field to electrons on the honeycomb lattice, we have:

$$\mathcal{H}_0(\boldsymbol{A}_i) = -t\sum_{\boldsymbol{R}_i}\sum_{n=1}^{3}\Big(a^\dagger(\boldsymbol{R}_i)b(\boldsymbol{R}_i+\boldsymbol{\delta}_n)\mathrm{e}^{-i\boldsymbol{\delta}_n\cdot\boldsymbol{A}_i}+h.c.\Big), \tag{A1}$$

with A the unit cell area. Here, the electron charge has been set to unity. Taylor expanding to linear order gives

$$\mathcal{H}_0(\boldsymbol{A}_i) = \mathcal{H}_0 - A\sum_{\boldsymbol{R}_i}\boldsymbol{J}(\boldsymbol{R}_i)\cdot\boldsymbol{A}_i, \tag{A2}$$

$$\boldsymbol{J}(\boldsymbol{R}_i) = -i\frac{t}{A}\sum_{n=1}^{3}\big[a^\dagger(\boldsymbol{R}_i)b(\boldsymbol{R}_i+\boldsymbol{\delta}_n) - b^\dagger(\boldsymbol{R}_i+\boldsymbol{\delta}_n)a(\boldsymbol{R}_i)\big]. \tag{A3}$$

Within time-dependent perturbation theory, the current-density at site $\boldsymbol{R}_i$ is:

$$\langle J_\mu(\boldsymbol{R}_i,t)\rangle = A\int_{-\infty}^{\infty}dt'\sum_{\boldsymbol{R}_j}\chi_{J,\mu,\nu}(\boldsymbol{R}_i,\boldsymbol{R}_j;t-t')A_\nu(\boldsymbol{R}_j), \tag{A4}$$

$$\chi_{J,\mu,\nu}(\boldsymbol{R}_i,\boldsymbol{R}_j;t-t') = i\Theta(t-t')\big\langle\big[J_\mu(\boldsymbol{R}_i,t),J_\nu(\boldsymbol{R}_j,t')\big]\big\rangle, \tag{A5}$$

where in the second line we defined the retarded current-current correlator. Assuming the vector potential is uniform and has the time-dependence $\mathbf{A}(t) = \frac{e^{-i\omega t}}{i\omega}\mathbf{E}$, with $\mathbf{E}$ the electric field, we find

$$\langle J_\mu\rangle = \sigma_{\mu\nu}E_\nu, \tag{A6}$$

$$\sigma_{\mu\nu}(\omega) = \frac{1}{\omega}\chi_{J,\mu,\nu}(\omega), \tag{A7}$$

where $\chi_{J,\mu,\nu}(\omega)$ is the spatial and temporal Fourier transform of Eq. (A5). The Eq. (A7) for the optical conductivity is equivalent to Eq. (26). As usual, this quantity can be obtained from the corresponding Matsubara function

$$\chi_{J,\mu,\nu}(i\Omega) = \frac{1}{NA}\int_0^\beta d\tau\mathrm{e}^{i\Omega\tau}\langle J_\mu(\tau)J_\nu(0)\rangle. \tag{A8}$$

In this formula N is the number of Bravais lattice points, A is the unit cell area, and $\beta = \frac{1}{k_\mathrm{B}T}$ (although we always work in the zero-temperature limit). Here, $J_\mu(\tau)$ is given by Eq. (8). Henceforth, we shall drop the subscript μ,ν in the definition of $\chi_{J,\mu,\nu}(i\Omega)$, which we need for the case of $\mu=\nu$.

1. Bare-bubble diagram

To compute the conductivity, we need to evaluate $\chi_{J,\mu,\nu}(i\Omega)$ to leading order in perturbation theory. We start with the zeroth order result, which is the "bare-bubble" diagram, Fig. 2 (a) of the main text. Setting $\mu=\nu=y$ yields:

$$\chi_J^{(0)}(i\Omega) = -T\sum_{\mathbf{k},\omega}\mathrm{Tr}\big[\hat{J}_{y,\boldsymbol{k},0}G_{\boldsymbol{k},i\omega}\hat{J}_{y,\boldsymbol{k}}G_{\boldsymbol{k},i\omega+i\Omega}\big] \tag{A9}$$

$$= -\sum_{\mathbf{k}}\frac{\Big[h^*_{\boldsymbol{k}}j_{y,\boldsymbol{k}} - h_{\boldsymbol{k}}j^*_{y,\boldsymbol{k}}\Big]^2}{t\ |h_{\boldsymbol{k}}|(4|h_{\boldsymbol{k}}|^2+\Omega^2/t^2)}. \tag{A10}$$

Here, $\hat{J}_\mu(\boldsymbol{k})$ is defined in Eq. (8) and in the second line we evaluated the frequency integration and the trace. Next we rewrite the current-component $j_y(\boldsymbol{k})$, defined in Eq. (10), as:

$$j_{y,\boldsymbol{k}} = \frac{-ita}{2}\left[h_{\boldsymbol{k}}-3\right] \tag{A11}$$

$$j^*_{y,\boldsymbol{k}} = \frac{ita}{2}\left[h^*_{\boldsymbol{k}}-3\right]\ , \tag{A12}$$

and obtain for our retarded current correlator:

$$\chi_J^{(0)}(i\Omega) = \frac{ta^2}{4}\sum_{\mathbf{k}} \frac{18|h_{\boldsymbol{k}}|^2 + 4|h_{\boldsymbol{k}}|^4 - 12|h_{\boldsymbol{k}}|^2\left(h_{\boldsymbol{k}} + h_{\boldsymbol{k}}^*\right) + 9\left(h_{\boldsymbol{k}}^2 + h_{\boldsymbol{k}}^{*2}\right)}{|h_{\boldsymbol{k}}|(4|h_{\boldsymbol{k}}|^2 + \Omega^2/t^2)}. \tag{A13}$$

Upon analytically continuing $i\Omega \to \omega + i\delta$,

$$\frac{1}{4|h_{\boldsymbol{k}}|^2 + \Omega^2} \to \text{P.V.}\frac{1}{4|h_{\boldsymbol{k}}|^2 - \omega^2} + i\frac{\pi}{2\omega}\delta(\omega - 2|h_{\boldsymbol{k}}|), \tag{A14}$$

with P.V. denoting the principal value (and we assumed $\omega > 0$) and taking the imaginary part, we obtain the retarded correlator:

$$\chi_J^{(0)}(\omega) = \sum_{\boldsymbol{k}}\left(\frac{ta^2\pi}{32}\right)\left[18 + 4|h_{\boldsymbol{k}}|^2 + 18\frac{[\Re h_{\boldsymbol{k}}]^2 - [\Im h_{\boldsymbol{k}}]^2}{|h_{\boldsymbol{k}}|^2} - 24[\Re h_{\boldsymbol{k}}]\right]\delta\left(|h_{\boldsymbol{k}}| - \frac{\omega}{2t}\right) \tag{A15}$$

$$= \sum_{\boldsymbol{k}}\left(\frac{ta^2\pi}{32}\right) g\left(h_{\boldsymbol{k}}\right)\ \delta\left(|h_{\boldsymbol{k}}| - \frac{\omega}{2t}\right). \tag{A16}$$

In this expression, we have kept the dimensionful quantities a and t, although henceforth we shall set them to unity and measure the frequency relative to t. Due to the delta function constraint, we can integrate the above expression analytically. Therefore we split up the function $g\left(h(\boldsymbol{k})\right)$ into two functions and define:

$$g_1(|h_{\boldsymbol{k}}|) = 18 + 4|h_{\boldsymbol{k}}|^2 \tag{A17}$$

$$g_2\left(h_{\boldsymbol{k}}\right) = 18\frac{[\Re h_{\boldsymbol{k}}]^2 - [\Im h_{\boldsymbol{k}}]^2}{|h_{\boldsymbol{k}}|^2} - 24[\Re h_{\boldsymbol{k}}]\,. \tag{A18}$$

Firstly, we evaluate the expression:

$$\chi_{J,1}^{(0)}(\omega) = \frac{\pi}{16}\sum_k g_1(|h_{\boldsymbol{k}}|)\delta(2|h_{\boldsymbol{k}}| - \omega)\,. \tag{A19}$$

We introduce the density of state per unit cell as

$$\rho(E) = \sum_{\mathbf{k}}\delta(E - |h_{\boldsymbol{k}}|)$$

$$= \int\frac{d^2k}{(2\pi)^2}\sum_{i=1}^{4}\frac{1}{|\partial_{k_{x,i}}|h_{k_{x,i},k_y}||}\delta(k_x - k_{x,i}) \tag{A20}$$

with the $k_{x,i}$ being the solution to $E = |h_{\boldsymbol{k}}|$:

$$k_{x,1} = -\frac{2}{\sqrt{3}}\arccos\left[\frac{1}{4}(-2\cos\left(\frac{3k_y}{2}\right) - \sqrt{2}\sqrt{2E^2 - 1 + \cos\left(3k_y\right)})\right]$$

$$k_{x,2} = +\frac{2}{\sqrt{3}}\arccos\left[\frac{1}{4}(-2\cos\left(\frac{3k_y}{2}\right) - \sqrt{2}\sqrt{2E^2 - 1 + \cos\left(3k_y\right)})\right]$$

$$k_{x,3} = -\frac{2}{\sqrt{3}}\arccos\left[\frac{1}{4}(-2\cos\left(\frac{3k_y}{2}\right) + \sqrt{2}\sqrt{2E^2 - 1 + \cos\left(3k_y\right)})\right]$$

$$k_{x,4} = +\frac{2}{\sqrt{3}}\arccos\left[\frac{1}{4}(-2\cos\left(\frac{3k_y}{2}\right) + \sqrt{2}\sqrt{2E^2 - 1 + \cos\left(3k_y\right)})\right] \tag{A21}$$

describing curves that encircle the Dirac points at $\boldsymbol{k}_R = \frac{4\pi}{3a}(\frac{1}{2\sqrt{3}}\hat{x} + \frac{1}{2}\hat{y})$ and $\boldsymbol{k}_L = \frac{4\pi}{3a}(-\frac{1}{2\sqrt{3}}\hat{x} + \frac{1}{2}\hat{y})$ when the y component is restricted to $k_- < k_y < k_+$ with

$$k_\pm(E) = \frac{2\pi}{3} \pm \frac{\arccos\left(1 - 2E^2\right)}{3}\,. \tag{A22}$$

We can calculate the density of states analytically and obtain:

$$\rho(E) = \frac{1}{(2\pi)^2}\frac{32\ E\ \sqrt{1 - \frac{E}{3}}\ K\left[-\frac{16E}{(E-3)(1+E)^3}\right]}{3(3-E)(1+E)^{3/2}}\,, \tag{A23}$$

where $K[m]$ is the complete elliptic integral of the first kind. One part of the correlation function is thus given by:

$$\begin{aligned}\chi^{(0)}_{J,1}(\omega) &= \frac{\pi}{32}\sum_{\boldsymbol{k}} g_1(|h_{\boldsymbol{k}}|)\delta(|h_{\boldsymbol{k}}|-\omega/2) \\ &= \frac{\pi}{32}\rho\left(\frac{\omega}{2}\right) g\left(\frac{\omega}{2}\right) \\ &= \frac{\pi}{32}\rho\left(\frac{\omega}{2}\right)(18+\omega^2)\,. \end{aligned} \tag{A24}$$

In order to evaluate the expression:

$$\chi^{(0)}_{J,2}(\omega) = \frac{\pi}{16}\sum_{k} g_2(h_{\boldsymbol{k}})\delta(2|h_{\boldsymbol{k}}|-\omega)\,, \tag{A25}$$

we expand the above formula near the node, $h(\boldsymbol{k}_R+\boldsymbol{k})$, and write the deviation from the node in polar coordinates $\boldsymbol{k}=(k,\theta)$,

$$|h_{\boldsymbol{k}_R+\boldsymbol{k}}| \simeq \frac{3}{128}k(64-7k^2+16k\cos 3\theta - k^2\cos 6\theta), \tag{A26}$$

valid to $\mathcal{O}(k^3)$. The approximate solution to $\omega = 2|h_{\boldsymbol{k}_R+\boldsymbol{k}}|$ is:

$$k_1(\theta,\omega) = \frac{1}{3}\omega - \frac{1}{36}\omega^2\cos 3\theta + \frac{1}{1728}[7+8\cos^2 3\theta+\cos 6\theta]\omega^3\,, \tag{A27}$$

that is valid to $\mathcal{O}(\omega^3)$. The factor $g_2(h(\boldsymbol{k}))$ is, to the same order,

$$\begin{aligned} g_2(\boldsymbol{k}_R+\boldsymbol{k}) \simeq \frac{9}{32}[&k^3(-\cos 11\theta) + 3\left(5k^2-16\right)k\cos\theta + \left(64-20k^2\right)\cos 2\theta \\ &+ 2k\left(2\left(k^2-16\right)\cos 3\theta - 8(\cos 5\theta + 3k) + k(8\cos 4\theta + 8\cos 6\theta + 3k\cos 5\theta + 2\cos 8\theta(1-2k\cos\theta))\right)]\,. \end{aligned} \tag{A28}$$

From the delta function, we'll also need

$$\frac{d}{dk}|h_{\boldsymbol{k}_R+\boldsymbol{k}}| = \frac{3}{64}\left(64+32k\cos 3\theta - 21k^2 - 3k^2\cos 6\theta\right)\,. \tag{A29}$$

Then, assuming the same contribution comes from each node (which we have verified), we'll have:

$$\chi^{(0)}_{J,2}(\omega) = \frac{\pi}{8}\int_0^{2\pi} d\theta \int_0^{\infty} dk\ k\ g_2(\boldsymbol{k})\delta(2|h_{\boldsymbol{k}}|-\omega) \tag{A30}$$

$$= \frac{\pi}{8}\int_0^{2\pi} d\theta\ k_1(\theta,\omega)\frac{1}{|\frac{d}{dk_1}2|h_{\boldsymbol{k}_R+\boldsymbol{k}_1}||}g_2(\boldsymbol{k}_R+\boldsymbol{k}_1)\,, \tag{A31}$$

where we evaluated the radial k integral. To evaluate the integral, we simply insert $k_1(\theta,\omega)$ into the factors Eq. (A29) and Eq. (A30), insert them into the integrand and Taylor expand order by order in ω before evaluating the angle integrations. We obtain:

$$\chi^{(0)}_{J,2}(\omega) = -\frac{\omega}{8}\frac{\omega^2}{36}\,. \tag{A32}$$

Upon inserting the combined result into Eq. (A7), we find the frequency-dependent conductivity plotted in Fig. 6 and given by the formula:

$$\sigma(\omega) = \frac{\pi}{32\omega}\rho\left(\frac{\omega}{2}\right)(18+\omega^2) - \frac{1}{8}\frac{\omega^2}{36} \tag{A33}$$

$$\approx \sigma_0\left(1+\frac{1}{9}\omega+\mathcal{O}(\omega^3)\right)\,, \tag{A34}$$

with σ_0 the zero-frequency limit (reinserting correct factors of e^2 and $\hbar$, previously set to unity).

$$\sigma_0 = \frac{1}{8}\frac{e^2}{\hbar}. \tag{A35}$$

In comparing to the known result for the conductivity of N species of Dirac fermions, $\sigma_0 = \frac{N}{16}\frac{e^2}{\hbar}$, recall that here we have $N=2$, since we are considering the spinless case (but have summed over two nodes).

2. Interaction corrections to the conductivity

The leading order interaction corrections to the conductivity, that are linear order in the effective fine structure constant α, can be expressed in terms of self-energy (diagrams b and c) and vertex type (diagram d) Feynman diagrams, as depicted in Fig. 2 (a) and (b) of the main text. The self-energy contribution is:

$$\chi_J^{(1,bc)}(i\Omega) = -2T\sum_{\boldsymbol{k},\omega} \mathrm{Tr}\big[G_{\boldsymbol{k},i\omega-i\Omega} J_{\mu\boldsymbol{k}} G_{\boldsymbol{k},i\omega}\Sigma(\boldsymbol{k}) G_{\boldsymbol{k},i\omega} J_{\mu\boldsymbol{k}}\big], \tag{A36}$$

with the overall 2 coming from there being two such diagrams. The vertex contribution is given by:

$$\chi_J^{(1,d)}(i\Omega) = \sum_{\boldsymbol{k}} \int \frac{d^2q}{(2\pi)^2} V(\boldsymbol{q}) \mathrm{Tr}\big[I_\mu(\boldsymbol{k},\Omega) M_{-\boldsymbol{q}} I_\mu(\boldsymbol{k}+\boldsymbol{q},-\Omega) M_{\boldsymbol{q}}\big], \tag{A37}$$

with

$$I_\mu(\boldsymbol{k},\Omega) = T\sum_{\omega} G_{\boldsymbol{k},i\omega} J_{\mu\boldsymbol{p}} G_{\boldsymbol{k},i\omega-i\Omega}. \tag{A38}$$

We emphasize that momentum summations are always over the Brillouin zone and $\boldsymbol{q}$ integrations are always over the entire 2D momentum space, an issue that was neglected in Ref. 20 (see Eq.(15) of this work). As in our calculation of the self-energy, a crucial simplification of Eqs. (A36) and (A37) will involve writing these in a way that allows us to analytically evaluate the $\boldsymbol{q}$ integration.

Before analyzing these results in the subsequent sections, we first recall the result for the bc and d contributions within the nodal approximation. In this approximation, regularizing the integrals by imposing a large momentum cutoff Λ on the Coulomb potential (a procedure which obeys the Ward identity[18]), we obtain:

$$\mathrm{Im}\chi_J^{(1,bc)}(\omega) = -\frac{1}{2}\alpha\omega\sigma_0 \ln\frac{8\Lambda v}{\omega}, \tag{A39}$$

with $v = 3ta/2\hbar$, and

$$\mathrm{Im}\chi_J^{(1,d)}(\omega) = \frac{1}{2}\alpha\omega\sigma_0\big[\ln\frac{8\Lambda v}{\omega} + \frac{19-6\pi}{6}\big], \tag{A40}$$

yielding the sum

$$\mathrm{Im}\chi_J^{(1,bc)}(\omega) + \mathrm{Im}\chi_J^{(1,d)}(\omega) = \sigma_0\alpha\frac{19-6\pi}{12}. \tag{A41}$$

These formulas for the bc and d contributions are of course approximately valid within the tight-binding theory, with the replacement of the UV cutoff $\Lambda \to 1/a$, so that we expect each contribution to go as $\sim \omega\ln\omega$. This creates numerical difficulties, as each term is large, requiring a cancellation to return the value that is consistent with the nodal result $\propto \frac{19-6\pi}{12} \simeq 0.0125$. However, as shown in the main text, our numerical calculations are indeed consistent with this value.

3. Diagrams b and c

Starting with Eq. (A36), we first evaluate the frequency integration and the trace. Then we find (summing over the xx and yy components and dividing by 2):

$$\chi_J^{(1,bc)}(i\Omega) = -\sum_{\mathbf{p}} \frac{1}{4|h_{\boldsymbol{p}}|^3}\Big[\frac{D_1(\boldsymbol{p})}{4|h_{\boldsymbol{p}}|^2+\Omega^2} + D_2(\boldsymbol{p})\frac{4|h_{\boldsymbol{p}}|^2-\Omega^2}{(4|h_{\boldsymbol{p}}|^2+\Omega^2)^2}\Big], \tag{A42}$$

where the functions $D_1(\boldsymbol{p})$ and $D_2(\boldsymbol{p})$ are given by:

$$D_1(\boldsymbol{p}) = 2\big(h^*\Sigma_{12} - h\Sigma_{21}\big)\big[(h^*)^2(j_x^2+j_y^2) - h^2((j_x^*)^2+(j_y^*)^2)\big], \tag{A43}$$

$$D_2(\boldsymbol{p}) = \big(h^*\Sigma_{12} + h\Sigma_{21}\big)\Big[(h^*)^2(j_x^2+j_y^2) + h^2((j_x^*)^2+(j_y^*)^2) - 2(j_xj_x^* + j_yj_y^*)|h|^2\Big] \tag{A44}$$

Although this expression is complicated, all that is left is to analytically continue $i\Omega \to \omega + i\delta$ and take the imaginary part. The analytic continuation can be performed using Eq. (A14) for the term proportional to $D_1(\boldsymbol{p})$ and

$$\frac{4|h|^2 - \Omega^2}{(4|h|^2+\Omega^2)^2} = \frac{d}{d\Omega}\frac{\Omega}{4|h|^2+\Omega^2} \to \frac{d}{d\omega}\frac{\omega}{4|h|}\Big[\frac{1}{2|h|+\omega+i\delta} + \frac{1}{2|h|-\omega-i\delta}\Big], \tag{A45}$$

for the term proportional to $D_2(\boldsymbol{p})$. After taking the imaginary part (and assuming $\omega > 0$), we have

$$\mathrm{Im}\chi_J^{(1,bc)}(\omega) = -\pi \sum_{\mathbf{p}} \frac{1}{16|h_{\boldsymbol{p}}|^4} D_1(\boldsymbol{p})\delta(\omega - 2|h_{\boldsymbol{p}}|) - \pi \frac{d}{d\omega}\sum_{\mathbf{p}} \frac{\omega}{16|h_{\boldsymbol{p}}|^4} D_2(\boldsymbol{p})\delta(\omega - 2|h_{\boldsymbol{p}}|). \tag{A46}$$

To evaluate this, then, we determine $\Sigma_{12}(\boldsymbol{k})$ for $\boldsymbol{k}$ within the BZ by evaluating the summation over $\boldsymbol{R}$ for a large set of Bravais lattice vectors. With the delta function constraint, all that remains is a numerical integration over p along the curves $\omega = 2|h(\boldsymbol{p})|$ (which go around the Dirac nodes).

4. Diagram d

Next, we turn to Eq. (A37). Our first task is to evaluate Eq. (A38). We find:

$$I_\mu(\boldsymbol{p},\Omega) = \frac{1}{|h_{\boldsymbol{p}}|(4|h_{\boldsymbol{p}}|^2+\Omega^2)} V_\mu(\boldsymbol{p},\Omega), \tag{A47}$$

$$V_\mu(\boldsymbol{p},\Omega) \equiv \begin{pmatrix} \frac{1}{2}i\Omega\big[h_{\boldsymbol{p}} j^*_{\mu\boldsymbol{p}} - h^*_{\boldsymbol{p}} j_{\mu\boldsymbol{p}}\big] & h^2_{\boldsymbol{p}} j^*_{\mu\boldsymbol{p}} - |h_{\boldsymbol{p}}|^2 j_{\mu\boldsymbol{p}} \\ h^{*2}_{\boldsymbol{p}} j_{\mu\boldsymbol{p}} - |h_{\boldsymbol{p}}|^2 j^*_{\mu\boldsymbol{p}} & \frac{1}{2}i\Omega\big[h^*_{\boldsymbol{p}} j_{\mu\boldsymbol{p}} - h_{\boldsymbol{p}} j^*_{\mu\boldsymbol{p}}\big] \end{pmatrix}. \tag{A48}$$

Now, we have

$$\chi_J^{(1,d)}(i\Omega) = \int \frac{d^2q}{(2\pi)^2} V(\boldsymbol{q}) \sum_{\mathbf{p}} \frac{1}{|h_{\boldsymbol{p}}|(4|h_{\boldsymbol{p}}|^2+\Omega^2)} \frac{1}{|h_{\boldsymbol{p}+\boldsymbol{q}}|(4|h_{\boldsymbol{p}+\boldsymbol{q}}|^2+\Omega^2)} \times \mathrm{Tr}\big[V_\mu(\boldsymbol{p},\Omega) M_{-\boldsymbol{q}} V_\mu(\boldsymbol{p}+\boldsymbol{q},-\Omega) M_{\boldsymbol{q}}\big], \tag{A49}$$

which we now proceed to simplify. Recall that, in the *bc* diagram, we expressed the self-energy as a summation over Bravais lattice vectors, so that the $\boldsymbol{q}$ integration did not need to be performed numerically (i.e., it was performed analytically to yield the real-space Coulomb interaction). In the present case of Eq. (A49), we can perform a similar trick by first writing the integral as

$$\chi_J^{(1,d)}(i\Omega) = = \sum_{\mathbf{p}} \frac{1}{|h_{\boldsymbol{p}}|(4|h_{\boldsymbol{p}}|^2+\Omega^2)} \mathrm{Tr}\big[V_\mu(\boldsymbol{p},\Omega) Q_\mu(\boldsymbol{p},-\Omega)\big], \tag{A50}$$

$$Q_\mu(\boldsymbol{p},-\Omega) \equiv \int \frac{d^2q}{(2\pi)^2} V(\boldsymbol{q}) \frac{M_{-\boldsymbol{q}} V_\mu(\boldsymbol{p}+\boldsymbol{q},-\Omega) M_{\boldsymbol{q}}}{|h_{\boldsymbol{p}+\boldsymbol{q}}|(4|h_{\boldsymbol{p}+\boldsymbol{q}}|^2+\Omega^2)}, \tag{A51}$$

Much like the self-energy, we can express $Q_\mu(\boldsymbol{p},-\Omega)$ as a sum over Bravais lattice vectors of a summand for which the $\boldsymbol{q}$ integration may be performed analytically. The result is:

$$Q_\mu(\boldsymbol{p},-\Omega) = A\sum_{\boldsymbol{R}} \mathrm{e}^{i\boldsymbol{p}\cdot\boldsymbol{R}} \sum_{\mathbf{p}'} \mathrm{e}^{-i\boldsymbol{p}'\cdot\boldsymbol{R}} \begin{pmatrix} V_{\mu,11}(\boldsymbol{p}',-\Omega)\frac{e^2}{|\boldsymbol{R}|} & V_{\mu,12}(\boldsymbol{p}',-\Omega)\frac{e^2}{|\boldsymbol{R}-a\hat{y}|} \\ V_{\mu,21}(\boldsymbol{p}',-\Omega)\frac{e^2}{|\boldsymbol{R}+a\hat{y}|} & V_{\mu,22}(\boldsymbol{p}',-\Omega)\frac{e^2}{|\boldsymbol{R}|} \end{pmatrix} \frac{1}{|h_{\boldsymbol{p}'}|(4|h_{\boldsymbol{p}'}|^2+\Omega^2)}, \tag{A52}$$

which now involves a summation over Bravais lattice vectors and an integration over the BZ. Inserting this into, Eq. (A49), evaluating the trace, and simplifying, we find:

$$\chi_J^{(1,d)}(i\Omega) = e^2 A \sum_{\boldsymbol{R}} \sum_{\mathbf{p},\mathbf{p}'} \mathrm{e}^{i(\boldsymbol{p}-\boldsymbol{p}')\cdot\boldsymbol{R}} \frac{1}{|h_{\boldsymbol{p}}|(4|h_{\boldsymbol{p}}|^2+\Omega^2)} \frac{1}{|h_{\boldsymbol{p}'}|(4|h_{\boldsymbol{p}'}|^2+\Omega^2)} \times \Big[\frac{V_{\mu,11}(\boldsymbol{p},\Omega)V_{\mu,11}(\boldsymbol{p}',-\Omega) + V_{\mu,22}(\boldsymbol{p},\Omega)V_{\mu,22}(\boldsymbol{p}',-\Omega)}{|\boldsymbol{R}|} + \frac{V_{\mu,21}(\boldsymbol{p},\Omega)V_{\mu,12}(\boldsymbol{p}',-\Omega)}{|\boldsymbol{R}-a\hat{y}|} + \frac{V_{\mu,12}(\boldsymbol{p},\Omega)V_{\mu,21}(\boldsymbol{p}',-\Omega)}{|\boldsymbol{R}+a\hat{y}|}\Big]. \tag{A53}$$

The next step is to analytically continue, using Eq. (A14). For the imaginary part, we'll clearly have two terms, one with $\delta(\omega - 2|h(\boldsymbol{p})|)$ and one with $\delta(\omega - 2|h(\boldsymbol{p}')|)$. However, since the integrand is symmetric under exchanging $\boldsymbol{p}$ and

$\boldsymbol{p}'$ and also $\boldsymbol{R} \to -\boldsymbol{R}$, these two terms are identical. We finally obtain (summing over the xx and yy components and dividing by 2, and using Eq. (A48)) :

$$\chi_J^{(1,d)}(\omega) = -e^2 A \sum_{\mu=x,y} \sum_{\boldsymbol{R}} \sum_{\mathbf{p},\mathbf{p}'} \mathrm{e}^{i(\boldsymbol{p}-\boldsymbol{p}')\cdot\boldsymbol{R}} \left[h_{\boldsymbol{p}} j^*_{\mu\boldsymbol{p}} - h^*_{\boldsymbol{p}} j_{\mu\boldsymbol{p}}\right]\left[h_{\boldsymbol{p}'} j^*_{\mu\boldsymbol{p}'} - h^*_{\boldsymbol{p}'} j_{\mu\boldsymbol{p}'}\right] \times \left[\frac{\omega^2}{2|\boldsymbol{R}|} + \frac{h^*_{\boldsymbol{p}} h_{\boldsymbol{p}'}}{|\boldsymbol{R} - a\hat{y}|} + \frac{h_{\boldsymbol{p}} h^*_{\boldsymbol{p}'}}{|\boldsymbol{R} + a\hat{y}|}\right] \frac{\pi}{2\omega} \delta(\omega - 2|h_{\boldsymbol{p}}|) \frac{1}{|h_{\boldsymbol{p}}||h_{\boldsymbol{p}'}|} \mathrm{P.V.} \frac{1}{4|h_{\boldsymbol{p}'}|^2 - \omega^2}, \tag{A54}$$

the result for the retarded correlator. To evaluate this diagram, we must numerically evaluate the momentum integrations over the Brillouin zone and the summation over BL vectors $\boldsymbol{R}$. This result for point like Wannier functions can again be generalized to the case of the Coulomb potential given in Eq. (18). Upon substituting the expression $\frac{1}{|\boldsymbol{R}-a\hat{y}|}$ by $\sqrt{\frac{\pi}{2}}\frac{1}{\lambda} e^{-|\boldsymbol{R}-a\hat{y}|/4\lambda^2} I_0\left(\frac{|\boldsymbol{R}-a\hat{y}|^2}{4\lambda^2}\right)$ and analogously for $\frac{1}{|\boldsymbol{R}|}$ and $\frac{1}{|\boldsymbol{R}+a\hat{y}|}$, the nonzero width of the on-site Wannier function is taken into account.

Appendix B: Continuum RG/ Minimal subtraction scheme

Our starting point is the action of graphene:

$$S = \int d\tau \int d^{d_e}x \; \psi_0^\dagger \left(\partial_\tau + i e_0 A_0^0 + v_0(-i\boldsymbol{\nabla}\boldsymbol{\sigma})\right) \psi_0 + \int d\tau \int d^{d_\gamma}x \left(\partial_x A_0^0\right)^2 , \tag{B1}$$

where the subscript X_0 denotes the bare quantities. Here, d_e is the spatial dimensionality of the electron degrees of freedom (henceforth we call $d_e \to d = 2 - \epsilon$) and $d_\gamma = 3$ is the dimensionality of the gauge fields A_0 mediating the Coulomb potential. Taking a closer look at the action of graphene, we can derive the dimensionality of the fermionic fields and of the electrical charge. Since the action has to be a dimensionless quantity, we find for the ferminonic fields have the following dimensionality:

$$[\psi_0] = \frac{d_e}{2} , \tag{B2}$$

while the bosonic fields of the photons have the dimension:

$$[A_0^\mu] = 1 - \epsilon . \tag{B3}$$

We can now deduce from these conditions that the dimension of the electrical charge e_0 is given by:

$$[e_0] = \epsilon . \tag{B4}$$

We have seen in Eq. (B4) that the bare charge has dimensionality $[e_0] = \epsilon$. However, in order to have the electrical charge as a dimensionless quantity, we again introduce the parameter μ:

$$\frac{e_0^2}{\mu^{2\epsilon}} = e^2(\mu) Z_e \;\Leftrightarrow\; e_0^2 = \frac{e^2(\mu)}{4^\epsilon} e^{2\gamma\epsilon} \tilde{\mu}^{-2\epsilon} \;\Leftrightarrow\; e^2(\mu) = e_0^2 4^\epsilon e^{-2\gamma\epsilon} \tilde{\mu}^{-2\epsilon} . \tag{B5}$$

Upon recalling Eq. (41) and Eq. (45), we see that the velocity is renormalized by:

$$v_0 = \left[1 - \frac{1}{4\epsilon}\alpha(\mu)\right] v(\mu) , \tag{B6}$$

which can be rewritten as:

$$v(\mu) = \frac{4\epsilon v_0}{4\epsilon - \alpha(\mu)} . \tag{B7}$$

Now we can define our coupling constant as:

$$\alpha(\mu) = \frac{e^2(\mu)}{v(\mu)} . \tag{B8}$$

Combining the above equation with Eq. (B5) and Eq. (B7), we obtain for the coupling constant the following expression:

$$\alpha(\mu) = \frac{\alpha_0 4^\epsilon e^{-2\gamma\epsilon}\tilde{\mu}^{-2\epsilon}}{1 + \frac{\alpha_0}{4}\frac{1}{\epsilon}4^\epsilon e^{-2\gamma\epsilon}\tilde{\mu}^{-2\epsilon}} \,. \tag{B9}$$

Next we replace again the divergence by the logarithm, using $\frac{1}{\epsilon} \to \log(\mu/\omega)$, and than take the limit $\epsilon \to 0$. This yields:

$$\alpha(\omega) = \frac{\alpha_0}{1 + \frac{\alpha_0}{4}\log\left(\frac{\mu}{\omega}\right)} \,. \tag{B10}$$

Treating the velocity in an analogous way leads to:

$$v_0 = v(\mu) - \frac{1}{4\epsilon}e^2(\mu) \;\Rightarrow\; v(\mu) = v_0 + \frac{e_0^2}{4\epsilon}4^\epsilon e^{-2\gamma\epsilon}\tilde{\mu}^{-2\epsilon} \,. \tag{B11}$$

After replacing the divergence and taking the limit $\epsilon \to 0$, we obtain:

$$v(\omega) = v_0 + \frac{e_0^2}{4}\log\left(\frac{\mu}{\omega}\right) \,. \tag{B12}$$

[1] A. H. Castro Neto, F. Guinea, N. M. R. Peres, K. S. Novoselov, and A. K. Geim, Rev. Mod. Phys. **81**, 109 (2009).
[2] K. S. Novoselov, A. K. Geim, S. V. Morozov, D. Jiang, M. I. Katsnelson, I. V. Grigorieva, S. V. Dubonos, and A. A. Firsov, Nature **438**, 197 (2005).
[3] Y. Zhang, Y.-W. Tan, H. L. Stormer, and P. Kim, Nature **438**, 201 (2005).
[4] N. Stander, B. Huard, and D. Goldhaber-Gordon, Phys. Rev. Lett. **102**, 026807 (2009).
[5] X. Du, I. Skachko, F. Duerr, A. Luican, and E. Y. Andrei, Nature **462**, 192 (2009).
[6] K. I. Bolotin, F. Ghahari, M. D. Shulman, H. L. Stormer, and P. Kim, Nature **462**, 196 (2009).
[7] J. Crossno, J. K. Shi, K. Wang, X. Liu, A. Harzheim, A. Lucas, S. Sachdev, P. Kim, T. Taniguchi, K. Watanabe, T. A. Ohki, and K. C. Fong, Science **351**, 1058 (2016).
[8] M. Titov, R. V. Gorbachev, B. N. Narozhny, T. Tudorovskiy, M. Schütt, P. M. Ostrovsky, I. V. Gornyi, A. D. Mirlin, M. I. Katsnelson, K. S. Novoselov, A. K. Geim, and L. A. Ponomarenko, Phys. Rev. Lett. **111**, 166601 (2013).
[9] B. N. Narozhny, I. V. Gornyi, M. Titov, M. Schütt, and A. D. Mirlin, Phys. Rev. B **91**, 035414 (2015).
[10] U. Briskot, M. Schütt, I. V. Gornyi, M. Titov, B. N. Narozhny, and A. D. Mirlin, Phys. Rev. B **92**, 115426 (2015).
[11] D. A. Bandurin, I. Torre, R. K. Kumar, M. Ben Shalom, A. Tomadin, A. Principi, G. H. Auton, E. Khestanova, K. S. Novoselov, I. V. Grigorieva, L. A. Ponomarenko, A. K. Geim, and M. Polini, Science **351**, 1055 (2016).
[12] L. Levitov and G. Falkovich, Nat. Phys. **Adv. Online Publ.**, 1745 (2016).
[13] D. C. Elias, R. V. Gorbachev, A. S. Mayorov, S. V. Morozov, A. A. Zhukov, P. Blake, L. A. Ponomarenko, I. V. Grigorieva, K. S. Novoselov, F. Guinea, and A. K. Geim, Nat. Phys. **7**, 701 (2011).
[14] D. A. Siegel, C.-H. Park, C. Hwang, J. Deslippe, A. V. Fedorov, S. G. Louie, and A. Lanzara, Proc. Natl. Acad. Sci. **108**, 11365 (2011).
[15] G. L. Yu, R. Jalil, B. Belle, A. S. Mayorov, P. Blake, F. Schedin, S. V. Morozov, L. A. Ponomarenko, F. Chiappini, S. Wiedmann, U. Zeitler, M. I. Katsnelson, A. K. Geim, K. S. Novoselov, and D. C. Elias, Proc. Natl. Acad. Sci. **110**, 3282 (2013).
[16] I. F. Herbut, V. Juričić, and O. Vafek, Phys. Rev. Lett. **100**, 046403 (2008).
[17] E. G. Mishchenko, EPL **83**, 17005 (2008).
[18] D. E. Sheehy and J. Schmalian, Phys. Rev. B **80**, 193411 (2009).
[19] V. Juričić, O. Vafek, and I. F. Herbut, Phys. Rev. B **82**, 235402 (2010).
[20] B. Rosenstein, M. Lewkowicz, and T. Maniv, Phys. Rev. Lett. **110**, 066602 (2013).
[21] I. Sodemann and M. M. Fogler, Phys. Rev. B **86**, 115408 (2012).
[22] G. Gazzola, A. L. Cherchiglia, L. A. Cabral, M. C. Nemes, and M. Sampaio, EPL **104**, 27002 (2013).
[23] S. H. Abedinpour, G. Vignale, A. Principi, M. Polini, W.-K. Tse, and A. H. MacDonald, Phys. Rev. B **84**, 045429 (2011).
[24] A. Golub and B. Horovitz, Phys. Rev. B **81**, 245424 (2010).
[25] R. R. Nair, P. Blake, A. N. Grigorenko, K. S. Novoselov, T. J. Booth, T. Stauber, N. M. R. Peres, and A. K. Geim, Science **320**, 1308 (2008).
[26] D. N. Basov, R. D. Averitt, D. van der Marel, M. Dressel, and K. Haule, Rev. Mod. Phys. **83**, 471 (2011).
[27] A. W. W. Ludwig, M. P. A. Fisher, R. Shankar, and G. Grinstein, Phys. Rev. B **50**, 7526 (1994).
[28] J. Gonzalez, F. Guinea, and M. Vozmediano, Nucl. Phys. B **424**, 595 (1994).

[29] D. E. Sheehy and J. Schmalian, Phys. Rev. Lett. **99**, 226803 (2007).
[30] T. Stauber, N. M. R. Peres, and A. K. Geim, Phys. Rev. B **78**, 085432 (2008).
[31] B. Rosenstein, H. C. Kao, and M. Lewkowicz, Phys. Rev. B **90**, 045137 (2014).
[32] F. de Juan, A. G. Grushin, and M. A. H. Vozmediano, Phys. Rev. B **82**, 125409 (2010).
[33] S. Teber and A. V. Kotikov, EPL **107**, 57001 (2014).
[34] G. D. Mahan, *Many-particle physics* (Kluwer Academic/Plenum Publishers, New York, N.Y., USA, 2000).
[35] J. H. Grönqvist, T. Stroucken, M. Lindberg, and S. W. Koch, Eur. Phys. J. B **85**, 395 (2012).
[36] M. E. Peskin and D. V. Schroeder, *An introduction to Quantum Field Theory* (Westview Press, Boulder, CO, 1995).
[37] K. Damle and S. Sachdev, Phys. Rev. B **56**, 8714 (1997).
[38] D. L. Boyda, V. V. Braguta, M. I. Katsnelson, and M. V. Ulybyshev, ArXiv e-prints (2016), arXiv:1601.05315 [cond-mat.str-el].